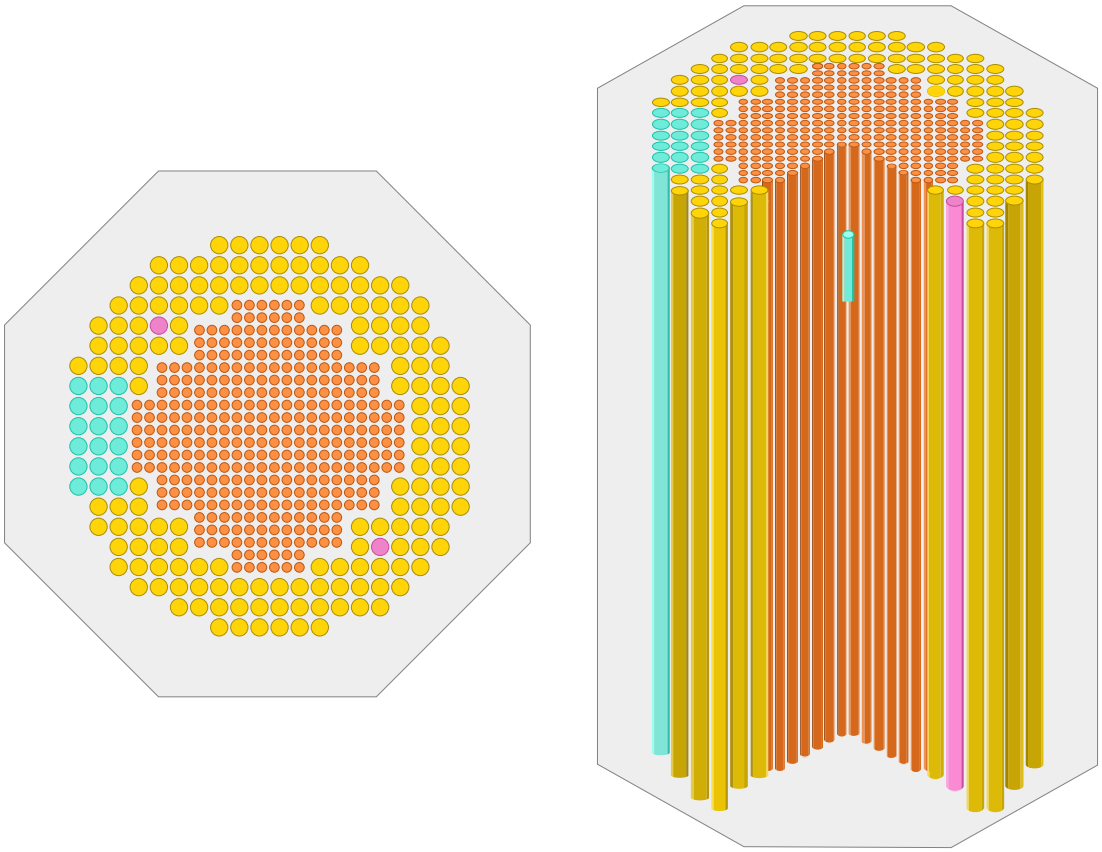

Modelling and Simulations of Neutron Noise Experiments

Master's thesis in Physics

TESS ELLERTSSON
AMANDA GOOLD

DEPARTMENT OF PHYSICS AND ASTRONOMY
CHALMERS UNIVERSITY OF TECHNOLOGY
Gothenburg, Sweden 2026
www.chalmers.se

Master's thesis 2026

Modelling and Simulations of Neutron Noise Experiments

TESS ELLERTSSON

AMANDA GOOLD

UNIVERSITY OF GOTHENBURG

CHALMERS
UNIVERSITY OF TECHNOLOGY

Reactor Physics, Modelling and Safety Group
Division of Subatomic, High-Energy and Plasma Physics
Department of Physics and Astronomy
Chalmers University of Technology
University of Gothenburg
Gothenburg, Sweden 2026

Modelling and Simulations of Neutron Noise Experiments
TESS ELLERTSSON
AMANDA GOOLD

Supervisor: Paolo Vinai, Antonio Galia
Examiner: Paolo Vinai, Mats Granath

MASTER'S THESIS 2026
Department of Physics and Astronomy
Division of Subatomic, High-Energy and Plasma Physics
Reactor Physics, Modelling and Safety Group
Chalmers University of Technology
SE-412 96 Gothenburg
Sweden
Telephone +46 31 772 1000

Cover: COLIBRI and POLLEN perturbation facilities in the CROCUS reactor corresponding to the third experimental campaign. The yellow and orange pins represent the outer and inner fuel, the pink the control rod guide tubes, and the blue pins show the oscillating fuel rods and absorber.

Typeset in LaTeX
Gothenburg, Sweden 2026

Modelling and Simulations of Neutron Noise Experiments
TESS ELLERTSSON, AMANDA GOOLD
Department of Physics and Astronomy
Chalmers University of Technology & University of Gothenburg

Abstract

This thesis focuses on neutron noise, which can be used to detect anomalies in the core of light-water nuclear reactors. Neutron noise refers to the small, stationary fluctuations of the neutron flux around its nominal value. These fluctuations arise from processes in the core, and can be monitored and analysed through a technique called neutron noise diagnostics. By identifying deviations in the neutron noise, anomalies that may lead to safety issues can be detected at an early stage, allowing prompt actions to be taken to prevent potential accidents.

This work involved modelling neutron noise experiments performed in the CROCUS research reactor (EPFL) using the diffusion based neutron noise solver CORE SIM+. The reactor's response to two different noise sources was simulated: a laterally vibrating group of fuel rods and a vertically vibrating absorber rod. The former has been modelled and verified in previous studies, whereas the latter has not previously been studied using CORE SIM+. Given its novelty in this context, several modelling approaches were explored for the vertically vibrating absorber to gain insight into how this type of perturbation can be represented. In addition, the study evaluated two computational approaches for computing the noise: the direct and adjoint methods. The influence of the geometric dimensionality was also assessed by performing simulations of the vibrating fuel rods in both 2D and 3D. The resulting simulated noise fields were then compared to the experimentally measured noise to assess the performance of the simulations.

The simulations of the vibrating group of fuel rods resulted in a noise field with both a notable point-kinetic component, and a strong spatial component near the perturbation. The simulations of the vibrating absorber produced noise fields with highly localised spatial effects in the vicinity of the perturbation and a negligible point-kinetic contribution. When combined, features originating from both sources appeared in the simulated noise. The direct and adjoint approaches yielded consistent results across all simulations, and the 2D- and 3D-simulations of the vibrating fuel rods gave essentially identical outcomes. The solver accurately reproduces the neutron noise measured at detector positions farther from the sources where the point-kinetic component dominates, whereas near the sources where the spatial effects are significant the deviations from measurements are more pronounced. These discrepancies are partly linked to the underlying approximations of the solver, leading to inaccurate predictions of the spatial gradients near a perturbation. For the case of the vibrating absorber, these discrepancies also arise because the models used are not fully representative of the physics of the noise source. This calls for further efforts to improve the models describing the vertically vibrating absorber.

Keywords: Neutron noise, 2-group neutron diffusion, Reactor diagnostics, Fuel rod vibration, Absorber rod vibration, Neutron kinetics

Acknowledgements

When we both started working on this project, we knew close to nothing about neutron noise. Since then, we have read many books and articles, run countless simulations, and discussed neutron noise to the point where we started dreaming about it. Whenever we risked getting 'lost in the noise', our excellent supervisors Paolo Vinai and Antonio Galia were there to help us navigate the project. We owe a great deal to them both through their support and guidance.

We notably want to thank Antonio for providing us with a great foundation for the project, talking to him always left us feeling inspired about the next step to pursue. And we thank Paolo for not only expanding our knowledge on neutron noise but also Italian wines, for making working on this project especially enjoyable, and for reminding us that Rome was not built in a day.

We also express our warmest gratitude to the staff at EPFL for providing both experimental data and the macroscopic cross section data used to model the CROCUS reactor, without which this project would not have been made possible.

Last but not least, we thank our families and loved ones for all the support and encouragement.

Tess Ellertsson & Amanda Goold, Gothenburg, June 2026

Contents

List of Figures

List of Tables

1

Introduction

Nuclear energy emerged from a series of findings in the early 20th century, ultimately leading to the theoretical explanation of fission in the year 1939 [1]. By splitting a heavy nucleus into lighter fission fragments, scientists revealed the tremendous amount of energy bound within the atomic nucleus. These developments sparked activity among researchers, who later found that in addition to energy being released, fission also results in the release of additional neutrons which can cause fission in surrounding nuclei. This results in a self-sustaining chain of reactions within fractions of a second, generating enormous amounts of energy in the form of heat and radiation.

The self-sustained chain of fission reactions is the underlying physical mechanism that enables power generation in nuclear power plants, where the power is generated by fissioning uranium-235. The emission of extra neutrons is essential for maintaining this chain reaction, as the emitted neutrons can trigger fission in neighbouring nuclei through collisions. Thus, each fission event yields a new generation of neutrons that can induce further fission. For a nuclear reactor to maintain a steady release of energy, the rate at which neutrons are produced through fission must be countered by absorption and leakage of neutrons from the system. Under such conditions, the system is in steady-state operation, referred to as being *critical*. When the production of neutrons exceeds the losses, the system becomes *supercritical* and energy production accelerates. When losses exceed production, the system becomes *subcritical* and energy production decreases [2].

In a nuclear power plant, the energy released through fission is ultimately used to produce steam that activates power generating turbines. The energy is initially deposited as heat in fuel pins grouped together in fuel assemblies. The fuel pins are surrounded by a circulating fluid known as the *reactor coolant* [3, p.3], with the primary purpose of absorbing and transporting heat from the core. A common type of nuclear reactor is the light water reactor (LWR), in which light water is used as the reactor coolant. There are two primary types of LWRs: boiling water reactors (BWR) and pressurised water reactors (PWR), both of which are *thermal reactors*. In BWRs, the heat generated through fission brings the coolant to boil, producing steam which drives the turbines, whereas in PWRs, the heat in transferred from the coolant to a secondary loop via a heat exchanger, and the steam produced in the secondary loop drives the turbines.

In LWRs, the water circulating through the core channels acts as both coolant and *moderator*, in which neutrons are slowed down through collisions with hydrogen in the water. The water also helps minimize neutron leakage by reflecting escaping neutrons back to the core. Neutrons emitted through fission are *fast neutrons*, which typically have energies ranging between 0.1 – 10 MeV. However, the probability of uranium-235 to undergo fission is significantly higher for *thermal neutrons* whose energies fall below 1 eV [2]. By slowing down the fast neutrons to thermal energies, the fission rate, and consequentially the power, increases. This process is necessary for sustaining the reaction chain in thermal reactors. To help balance the neutron population, control rods are used to absorb neutrons, leading to a decrease in neutron production and power. The control rods are made of materials capable of absorbing neutrons without themselves decaying, e.g Boron or Cadmium. The control rods are also used to immediately shut down the reactor if required.

Nuclear power has been used for electricity purposes since the 1950s, with the start-up of the first full-scale commercial nuclear electric generating plant in year 1956 in England [2]. As of today, there are over 400 operating nuclear power reactors across 32 countries, and LWR make up the vast majority of the world's reactor fleet [4], [5]. There are currently six nuclear reactors operating in Sweden, providing 7011 MW(e) and approximately 30% of the electricity [6]. These figures are expected to increase, following several recent initiatives concerning nuclear power to meet the growing demand for electricity in Sweden and globally. In November 2023, the Swedish government released a roadmap outlining the development of nuclear power production, promoting massive expansion of nuclear power by year 2045, with plans to construct two large-scale reactors by year 2035 [7]. In December 2023, several countries, including Sweden, France, Great Britain and USA pledged through the declaration Triple Nuclear Energy to strengthen collaboration between countries in the field of nuclear energy, and to work towards the collective goal of tripling the global nuclear power capacity by year 2050 [8].

The aspect of nuclear safety has always been of upmost importance, however, following recent initiatives to advance nuclear energy production, this issue becomes increasingly significant. Moreover, approximately 60% of the world's current reactor fleet consists of units that are older than 30 years, making operational complications more likely to occur [9]. To ensure safe operation, various actions and mitigation measures can be implemented. One such technique is neutron noise based diagnostics for core monitoring. Here, *neutron noise* refers to the stationary fluctuations of the neutron flux around its nominal value which arise from perturbations in the core composition. These fluctuations can be used to monitor the system and diagnose anomalies that could potentially lead to safety issues. The anomaly, or *noise source*, can be described in terms of class, location and characteristics. The classification of the noise source involves identifying the underlying phenomenon responsible for the noise, such as e.g. mechanical vibrations of core components or variations in coolant temperature. The localization entails determining which core regions are affected by the perturbation. Lastly, the characterisation tasks provides information on its magnitude and phase.

Nuclear power plants are inherently complex systems, and the inaccessibility of the core make them difficult to study and monitor. This makes neutron noise diagnostics a promising technique, as it is a non-intrusive approach that relies on online neutron flux measurements that do not interfere with normal operations. However, interpreting the data and understanding the underlying physical mechanisms becomes a challenging task that requires additional tools. Numerical tools are valuable resources for this purpose, as they offer the ability to simulate the reactor's behaviour in a controlled manner. Such tools require extensive validation against experimental data to ensure reliable results. Thus, measurements from real reactors play a crucial role in the development of numerical neutron noise simulators.

1.1 Thesis background

This section provides the background necessary for the remainder of the thesis. Starting with the research project CORTEX and the CROCUS neutron noise experiments, which are central to this work. Then, the neutron noise simulator CORE SIM+ used throughout the thesis is introduced, and previous research is briefly summarized. Lastly, the aims, objectives, limitations and thesis outline are stated.

1.1.1 The CORTEX project and CROCUS experiments

The European Horizon 2020 CORTEX project (where CORTEX stands for CORe monitoring Techniques and EXperimental validation and demonstration), is a research project coordinated by Chalmers University of Technology, gathering 20 partners from 11 countries from across Europe [9], carried out between the years 2017 – 2021. The main objectives of CORTEX were to develop simulation tools dedicated to modelling neutron noise in reactors, perform experiments to generate validation data, and to develop diagnostics algorithms that could be used to identify core anomalies from real measurements [10].

For the purpose of producing experimental data for validation, a series of measurement campaigns were carried out in two research reactors: CROCUS and AKR-2. This thesis focuses on the simulations of the CROCUS experiments. CROCUS is a zero-power reactor located at the École Polytechnique Fédérale de Lausanne (EPFL) in Switzerland [11]. Two types of noise sources were implemented: a group of laterally vibrating fuel rods, and an axially vibrating absorber, henceforth referred to as COLIBRI and POLLEN, respectively. Neutron detectors of various types and models where placed at in-core positions as well as in the water surrounding the core. Below is a brief overview of the campaigns:

- Campaign 1 [12] took place on 17 – 21 October 2018 and involved 20 measurements using a COLIBRI noise source, with a total of 11 neutron detectors distributed in the reactor.

- Campaign 2 [13] was conducted on 9 – 22 October 2019, where 31 measurements were carried out using the same COLIBRI noise source. This campaign

focused on the reduction of uncertainties compared to the first campaign, by e.g. improving the statistics through increased measurement times. They also increased the number of detectors to 15 and rearranged their positions.

- Campaign 3 [14] was carried out between 4 – 17 March 2021, where focus was put on the repetition of measurements from previous campaigns, as well as enhancing the spatial dependence of the noise by introducing the POLLEN noise source. This campaign consisted of 38 measurements in which COLIBRI and POLLEN devices were applied both separately and together. A total of 18 detectors were implemented in the system, some of which were rearranged with respect to previous campaigns.

1.1.2 The neutron noise solver CORE SIM+

There are several numerical solvers available for simulating the neutron noise in a reactor. Depending on the solver, the solution is given in either the time- or frequency domain, including or excluding non-linear terms, with different spatial resolutions, and with a deterministic or probabilistic approach. An overview of available solvers is provided in [15]. One defining feature is the underpinning theory of the solver, typically transport- or diffusion theory. Transport-based solvers rely on a higher-order approximation of the neutron transport equation resolving the angular dependence of the neutron flux. Diffusion based solvers employ the diffusion approximation to the transport equations, effectively neglecting the angular dependence. While transport theory might give a more accurate description of the neutron flux distribution, diffusion based solvers are generally more efficient in terms of computational costs [16].

The solver central to this thesis is CORE SIM+, a diffusion based neutron noise solver developed at Chalmers University of Technology [17]. It evolved from its predecessor CORE SIM [18], released in 2011. The development of CORE SIM+ was motivated by the need for numerical tools able to efficiently simulate the response of LWRs to neutron noise sources.

CORE SIM+ is a deterministic solver based on the two-group kinetic diffusion equations, and is designed to provide efficient numerical solutions to various neutron noise problems in 1D, 2D or 3D. It is coded in MATLAB, where the dynamic equations are solved in the frequency domain only for the oscillatory frequency of the noise source. CORE SIM+ simulates the response to a given noise source across the whole domain. More recently, a capability was added to compute the response at specific locations within the core via an adjoint approach. Its efficiency stems from the ability of using a non-uniform computational mesh, allowing the user to add a finer mesh in regions surrounding highly localised sources where the neutron flux gradient can be large. By adding mesh refinements in informative areas while letting less informative regions remain coarse, the discretization of the domain can be optimized and the computational efforts minimized.

1.1.3 Previous work

In an initial study by Mylonakis et al. [19], experimental data from the COLIBRI experiments carried out at CROCUS during the first measurement campaign of the CORTEX project was compared to CORE SIM+ simulations of the same experiment. The authors successfully reproduced the main trend of the measured data, along with the reactor response at some detector locations. They found that the overall spatial dependence of the neutron noise amplitude with respect to the static neutron flux was well reproduced by the solver. In a subsequent study, Mylonakis et al. [17] continued their analysis of the Campaign 1 experiments using CORE SIM+. They reported that the simulated reactor response was generally in reasonable agreement with the data, but with notable discrepancies for some detectors.

In the final validation report of the CORTEX project [20], the authors compared measured noise from both Campaigns 1 and 2 with predictions from several solvers. They found that the solvers predict a similar behaviour of the neutron noise, and note that the simulated amplitude of the noise increases at detector positions near the noise source. Furthermore, the diffusion-based solvers, including CORE SIM+, produce similar results, which are also in good agreement with some non-diffusion solvers. Generally, the simulated data from all solvers share similar trends with the experimental data, but with larger discrepancies closer to the noise source.

All aforementioned studies found notable deviations between measured and CORE SIM+ simulated noise for detectors in the vicinity of the noise source. They argue that this discrepancy may arise from limitations in diffusion theory and its ability to accurately reflect neutron transport near a perturbation, a notion that has been explored previously [21], [22] and that remains uncertain.

1.2 Thesis aims and objectives

The aims of this thesis is to investigate the modelling of vibrating fuel rods and absorbers in the CROCUS reactor, and to simulate and analyze the neutron noise induced by the individual perturbations and their combination. In addition, different numerical approaches available in CORE SIM+ are compared in the context of the CROCUS experimental campaigns. In order to achieve this, the following objectives are established:

- Modelling and performing noise calculations of the experiments from the three campaigns carried out at the CROCUS reactor using CORE SIM+, and comparing the simulated results to the experimentally measured data. Extra emphasis is put on the third campaign, since it has not previously been studied with CORE SIM+.

- Exploring different modelling options for a POLLEN-like noise source that enhances the spatial component of the noise when used together with COLIBRI.

- Comparing the direct and adjoint approaches of simulating neutron noise, and investigating how two-dimensional and three-dimensional reactor models influence the simulations.

1.3 Limitations

The simulated perturbations will be limited to two classes: mechanical vibrations of fuel rods in the lateral direction (COLIBRI) and mechanical vibrations of a localized neutron absorber in the axial direction (POLLEN). A maximum of two independent noise sources will be considered at once. The oscillations of the COLIBRI source will include frequencies of 0.1 Hz and 1 Hz, while the POLLEN source is limited to 1 Hz, in accordance with the experimental campaigns. The detectors are not modelled as we do not have the required cross section data to do so. Instead, the neutron noise will be estimated at positions within the core that correspond to the physical detector locations in the experiments.

1.4 Thesis outline

The rest of this thesis is structured as follows: in Chapter 2, the theory that is foundational to CORE SIM+ and the noise simulations is presented. Chapter 3 explains the methodology and simulation framework, including descriptions of the CROCUS reactor and the conducted experiments, and the computational models of the reactor and the noise sources. In Chapter 4 the results are presented. For Campaigns 1 and 2, the simulated noise is compared to the experimental data. For Campaign 3, a more in-depth analysis of the noise distributions is presented before comparing the results to experiments. Finally, the conclusions and future outlooks are discussed in Chapter 5.

2

Theory

This chapter introduces the underlying theory which the noise solver CORE SIM+ is based upon. First, neutron balance, the diffusion approximation and two-group formalism is presented, which is used to express the neutron population in a reactor under steady-state and time-varying conditions. The first-order neutron noise is then defined, and the concept of the point-kinetic and spatial components explored, which are central to understanding and explaining the behaviour of noise. After this, the basics of adjoint noise theory is introduced, presenting an alternative framework to study neutron noise.

2.1 Fundamental quantities

Before diving deeper into the theory, some basic quantities need to be defined. These are expressed in Eqs. (2.1 – 2.5), followed by a brief description of each quantity [23, pp. 4–6].

$$\text{Angular density :} \quad N(\boldsymbol{r}, \boldsymbol{\Omega}, E, t) \tag{2.1}$$

$$\text{Neutron density :} \quad n(\boldsymbol{r}, E, t) = \int_{4\pi} N(\boldsymbol{r}, \boldsymbol{\Omega}, E, t) d\boldsymbol{\Omega} \tag{2.2}$$

$$\text{Angular flux :} \quad \Phi(\boldsymbol{r}, \boldsymbol{\Omega}, E, t) = vN(\boldsymbol{r}, \boldsymbol{\Omega}, E, t) \tag{2.3}$$

$$\text{Scalar flux :} \quad \phi(\boldsymbol{r}, E, t) = \int_{4\pi} \Phi(\boldsymbol{r}, \boldsymbol{\Omega}, E, t) d\boldsymbol{\Omega} = vn(\boldsymbol{r}, E, t) \tag{2.4}$$

$$\text{Neutron current density :} \quad \boldsymbol{J}(\boldsymbol{r}, E, t) = \int_{4\pi} \boldsymbol{\Omega} \Phi(\boldsymbol{r}, \boldsymbol{\Omega}, E, t) d\boldsymbol{\Omega} \tag{2.5}$$

Starting from Eq. (2.1), the neutron *angular density* $N(\boldsymbol{r}, \boldsymbol{\Omega}, E, t)$ is defined as the expected number of neutrons at position $\boldsymbol{r}$ with direction $\boldsymbol{\Omega}$ and energy E at a time t, per unit volume per unit solid angle and per unit energy. Integrating the angular density over all directions yields the direction independent *neutron density* $n(\boldsymbol{r}, E, t)$, where the integration over 4π signifies integration over all solid angles.

The *angular flux* $\Phi(\boldsymbol{r}, \boldsymbol{\Omega}, E, t)$ is then defined as the product of the angular density and neutron speed v. This quantity tells us the total distance travelled per unit time by neutrons at position $\boldsymbol{r}$ of energy E moving in the direction of $\boldsymbol{\Omega}$, per unit volume per unit solid angle per unit energy. Integrating the angular flux over all directions results in the *scalar flux* $\phi(\boldsymbol{r}, E, t)$ which instead corresponds to the total distance travelled per unit time regardless of direction. Lastly, the flow of neutrons is given by the *neutron current density vector* $\boldsymbol{J}(\boldsymbol{r}, E, t)$. This is a vectorial quantity that represents the net flow of neutrons per unit area and unit time, where the component normal to a surface gives the net rate of neutrons crossing that surface.

Cross sections

Another very central quantity are *cross sections*. These describe the various interactions of neutrons with target nuclei. The *microscopic cross section* for some interaction α acting on a nuclide of type X is denoted $\sigma_{\alpha,X}(E)$, and represents the interaction area per nucleus of that species [24, Sec. 2.2a]. Although this is not a physical area, it can be likened to the target area that a neutron has to hit in order to cause the interaction to occur. The 'larger' the target, the higher the probability that a neutron will collide with it. From this, the *macroscopic cross section* is defined as

$$\Sigma_\alpha(\boldsymbol{r}, E, t) = \sum_X \rho_X(\boldsymbol{r}, t)\sigma_{\alpha,X}(E) \tag{2.6}$$

where $\rho_X(\boldsymbol{r}, t)$ is the atom density of nuclei of type X [24, Eq. (2.7)]. The macroscopic cross section has dimensions of reciprocal unit length, and represents the probability of interaction per unit path length travelled by a neutron. The scalar flux $\phi(\boldsymbol{r}, E, t)$ defines the instantaneous rate at which neutrons travel, which characterizes their combined ability to undergo nuclear reactions at a point in space and time [25, pp. 121–122]. It is therefore useful to construct the following quantity

$$\Sigma_\alpha(\boldsymbol{r}, E, t)\phi(\boldsymbol{r}, E, t), \tag{2.7}$$

which corresponds to the rate at which interaction α occurs at position $\boldsymbol{r}$, time t and energy E, per unit volume and unit energy. Quantities on this form occur very frequently in the remaining theory, and are essential for expressing the neutron population in a reactor.

2.2 Neutron balance

One of the fundamental principles of reactor theory is the concept of *neutron balance*. At any point in space, the change in the neutron population must be accounted for by physical processes that either produce, remove or displace neutrons [26, Sec. 5.3]. In simple terms,

$$\text{Change} = \text{Production} - \text{Disappearance} - \text{Leakage of neutrons}. \tag{2.8}$$

Expressing the relation in terms of direction-integrated reactor quantities results in the following neutron balance equation,

$$\frac{1}{v}\frac{\partial}{\partial t}\phi(\boldsymbol{r},E,t) = Q_0(\boldsymbol{r},E,t) - \Sigma_T(\boldsymbol{r},E,t)\phi(\boldsymbol{r},E,t) - \nabla\cdot\boldsymbol{J}(\boldsymbol{r},E,t). \tag{2.9}$$

Here, $Q_0(\boldsymbol{r},E,t)$ denotes the neutron source density, defined as the number of neutrons produced per unit volume, per unit energy, and per unit time. The disappearance of neutrons is described by the total macroscopic cross section $\Sigma_T(\boldsymbol{r},E,t)$, which represents the interactions of neutrons with the surrounding medium. This includes both neutron absorption and scattering events that may change the neutron energy. Finally, neutron leakage is represented by the neutron current density vector $\boldsymbol{J}(\boldsymbol{r},E,t)$. A derivation of this expression is presented in [27, pp. 124–125].

The diffusion approximation

At this point, the balance equation contains two unknowns: the scalar flux $\phi(\boldsymbol{r},E,t)$ and the neutron current density vector $\boldsymbol{J}(\boldsymbol{r},E,t)$. In order to make the equation solvable, a relationship between the two must be established. A common approach is to apply the *diffusion approximation*, which likens neutrons in a reactor to particles in a system undergoing chemical diffusion. In the context of reactor physics this translates to a net flow of neutrons from regions of higher neutron density to those of lower neutron density, described by Fick's law as [26, Eq. (5.8)]:

$$\boldsymbol{J}(\boldsymbol{r},E,t) = -D(\boldsymbol{r},E,t)\nabla\phi(\boldsymbol{r},E,t), \tag{2.10}$$

where $D(\boldsymbol{r},E,t)$ is a diffusion coefficient. Under this approximation, Eq. (2.9) becomes

$$\begin{aligned}\frac{1}{v}\frac{\partial}{\partial t}\phi(\boldsymbol{r},E,t) =& Q_0(\boldsymbol{r},E,t) - \Sigma_T(\boldsymbol{r},E,t)\phi(\boldsymbol{r},E,t)\\ &+ \nabla\cdot D(\boldsymbol{r},E,t)\nabla\phi(\boldsymbol{r},E,t).\end{aligned} \tag{2.11}$$

The use of the diffusion approximation is not exact and its validity is based on multiple assumptions. It is assumed that the approximation does not hold (i) in media that strongly absorbs neutrons, (ii) in the close vicinity of neutron sources, and (iii) if the scattering of neutrons is strongly anisotropic [25, Sec. 5-6].

Multi-group formalism

Neutrons are emitted over a continuous energy spectrum. However, to simplify calculations it is practical to divide the energy range into groups which together cover the entire distribution. This method is referred to as multi-group formalism [27, Ch. 7]. The groups are ordered in decreasing energy such that the most energetic neutrons belong to group $g = 1$, the next most energetic to group $g = 2$, and so on. Integrating and averaging the quantities in Eq. (2.11) over an energy group then results in the following expression [27, Eq. (7-17)]

$$\frac{1}{v_g}\frac{\partial}{\partial t}\phi_g(\boldsymbol{r},t) = Q_g(\boldsymbol{r},t) - \Sigma_{T,g}(\boldsymbol{r},t)\phi_g(\boldsymbol{r},t) + \nabla D_g(\boldsymbol{r},t)\nabla\phi_g(\boldsymbol{r},t), \tag{2.12}$$

where g denotes the energy group and v_g is the average neutron speed in that group. Both neutron absorption and scattering of neutrons between energy groups is still contained in Σ_T, and Q_g is used to denote neutron sources. This is the final form of the balance equation, referred to as the multi-group neutron diffusion equation.

In thermal reactors, at least two energy groups are needed to model the system, one for fast or high-energy neutrons produced from fission events ($g = 1$), and one which captures the slowing down of neutrons to thermal energies ($g = 2$) [26, p. 257]. From here on, two energy groups are considered, which is also the number of groups modelled in CORE SIM+.

2.2.1 Two-group steady-state diffusion theory

A nuclear reactor is said to be in steady-state if the neutron flux distribution is independent of time. In this case, the time derivative in Eq. (2.12) vanishes and the system reduces to a balance between neutron production and neutron losses. Under the two-group diffusion approximation the steady-state equations can then be written as[1] [27, Eq. (7-25)]

$$\begin{cases} \frac{1}{k_{\text{eff}}}[\nu\Sigma_{f,1,0}\phi_{1,0} + \nu\Sigma_{f,2,0}\phi_{2,0}] - [\Sigma_{a,1,0} + \Sigma_{r,0}]\phi_{1,0} + \nabla \cdot D_{1,0}\nabla\phi_{1,0} = 0 \\ -\Sigma_{a,2,0}\phi_{2,0} + \Sigma_{r,0}\phi_{1,0} + \nabla \cdot D_{2,0}\nabla\phi_{2,0} = 0 \end{cases} \tag{2.13}$$

If no external sources are present, neutron production is described by the macroscopic fission production terms $\nu\Sigma_{f,g,0}$. It is assumed that all fission neutrons are emitted as fast neutrons and thus only contribute to the fast group. The effective multiplication factor k_{eff} is a scaling parameter which ensures balance between production and losses. It is defined so that $k_{\text{eff}} = 1$ corresponds to a critical system, where neutron production exactly balances losses. If $k_{\text{eff}} < 1$ the system is subcritical and the neutron population decreases from generation to generation, while $k_{\text{eff}} > 1$ corresponds to a supercritical system with increasing neutron population [27, p. 76].

In both groups, $\Sigma_{T,g}$ is split into a macroscopic absorption cross section $\Sigma_{a,g,0}$ and the macroscopic removal cross section $\Sigma_{r,0}$, which is defined as

$$\Sigma_{r,0} = \Sigma_{s,1\to2,0} - \Sigma_{s,2\to1,0}\frac{\phi_{2,0}}{\phi_{1,0}}. \tag{2.14}$$

$\Sigma_{s,g\to g'}$ is in turn the macroscopic scattering cross section corresponding to scattering of neutrons from energy group g to g'. In light water reactors, up-scattering from thermal to fast energies is negligible, and the net contribution is therefore a transfer of fast neutrons to thermal energies. Finally, neutron leakage is expressed as previously, where the diffusion coefficients depend on the energy group. In matrix

[1] The explicit spatial dependence on $\boldsymbol{r}$ has been omitted in all of the terms. The subscript 0 denotes the steady-state.

form, Eq. (2.13) can be written compactly as [27, Eq. (7-26)]:

$$\begin{bmatrix} -\nabla \cdot D_{1,0}\nabla + \Sigma_{a,1,0} + \Sigma_{r,0} & 0 \\ -\Sigma_{r,0} & -\nabla \cdot D_{2,0}\nabla + \Sigma_{a,2,0} \end{bmatrix} \begin{bmatrix} \phi_{1,0} \\ \phi_{2,0} \end{bmatrix} = \frac{1}{k_{\text{eff}}} \begin{bmatrix} \nu\Sigma_{f,1,0} & \nu\Sigma_{f,2,0} \\ 0 & 0 \end{bmatrix} \begin{bmatrix} \phi_{1,0} \\ \phi_{2,0} \end{bmatrix} \tag{2.15}$$

With appropriate boundary conditions, this defines a generalized eigenvalue problem for the neutron flux distribution, which can also be expressed as

$$\mathcal{A}_0\boldsymbol{\phi}_0 = \frac{1}{k_{\text{eff}}}\mathcal{F}\boldsymbol{\phi}_0, \tag{2.16}$$

where $\mathcal{A}_0$ represents neutron loss processes in the steady-state system and $\mathcal{F}$ represents neutron production by fission.

2.2.2 Two-group time-dependent diffusion theory

While the steady-state formulation determines the time-independent distribution of the neutron flux, it does not account for time-varying effects in the reactor. Neutrons are both emitted immediately following fission events, so called prompt neutrons, as well as following the radioactive decay of fission fragments. Unlike prompt neutrons, these are emitted with a time delay, and are therefore referred to as delayed neutrons. The fission fragments responsible for this process are called precursors of delayed neutrons and are for thermal reactors typically divided into six groups, each collecting precursors with similar decay properties [27, p. 62]. In CORE SIM+, one group of precursors is used and the remaining theory will therefore be limited to a single group [17], [18].

Each decaying precursor eventually emits one neutron. The production of delayed neutrons is therefore determined by the precursor concentration $C(\boldsymbol{r}, t)$ together with the precursor decay constant λ [27, pp. 237–238]. The effective fraction of delayed neutrons β is defined as the number of delayed neutrons, divided by the total number of neutrons, both prompt and delayed [27, p. 63]. Inversely, the fraction of prompt neutrons is $(1 - \beta)$. Including delayed neutrons and precursor decay, the time-dependent two-group diffusion equations become[2] [27, Eq. (6-19)]

$$\begin{cases} \dfrac{1}{v_1}\dfrac{\partial}{\partial t}\phi_1 &= \nabla \cdot D_1\nabla\phi_1 - [\Sigma_{a,1} + \Sigma_r]\phi_1 + (1-\beta)\nu\Sigma_{f,1}\phi_1 \\ &\quad +(1-\beta)\nu\Sigma_{f,2}\phi_2 + \lambda C \\ \dfrac{1}{v_2}\dfrac{\partial}{\partial t}\phi_2 &= \nabla \cdot D_2\nabla\phi_2 - \Sigma_{a,2}\phi_2 + \Sigma_r\phi_1 \\ \dfrac{\partial}{\partial t}C &= \beta_i\nu\Sigma_{f,1}\phi_1 + \beta_i\nu\Sigma_{f,2}\phi_2 - \lambda C. \end{cases} \tag{2.17}$$

The first two equations describe the time-dependent neutron balance in the fast

[2] For simplicity, the explicit dependence on position $\boldsymbol{r}$ and time t has been omitted in all of the terms.

and thermal energy groups, respectively, while the third relation describes the time evolution of the precursor concentration. Although their energy spectra slightly differ, neutrons emitted from both prompt fission and precursor decay are assumed to contribute to the fast energy group.

2.3 Neutron noise theory

As shown in the previous sections, the neutron population in a reactor can be described by equations whose coefficients are given by macroscopic cross sections. In practice, the material properties of a reactor are not perfectly fixed. Perturbations to reactor properties, such as coolant density and temperature, or mechanical vibrations of reactor components induce fluctuations in the macroscopic cross sections. In turn, the fluctuations of the cross sections manifest as fluctuations in the neutron flux, commonly referred to as *neutron noise* [28, Sec. 3.1].

2.3.1 First-order neutron noise

The fluctuations of the neutron flux induced by the perturbations are assumed to be small and stationary around their expected mean values. Under normal, stable operating conditions, this mean state corresponds to the steady-state reactor. A time-dependent reactor quantity can thus be split into its expected steady-state value and fluctuations around that mean [28, Eq. (175)],

$$X(\boldsymbol{r},t) = X_0(\boldsymbol{r}) + \delta X(\boldsymbol{r},t). \tag{2.18}$$

Here, X is used to denote a generic reactor quantity, such as the macroscopic cross sections, neutron flux or precursor concentration. More formally, the fluctuations are assumed to be small compared to their means, and the processes stationary, respectively expressed as [28, Eqs. (176-177)]

$$\begin{aligned} |\delta X(\boldsymbol{r},t)| &\ll X_0(\boldsymbol{r}), \quad \forall(\boldsymbol{r},t) \\ \langle \delta X(\boldsymbol{r},t) \rangle &= 0, \quad \forall(\boldsymbol{r},t). \end{aligned} \tag{2.19}$$

Using the above definitions, the neutron noise balance equations are formulated analogous to the method shown in [28, Sec. 3.3.1]. First, all time-dependent terms in Eq. (2.17) are substituted for expressions on the form of Eq. (2.18). The only exception are the diffusion coefficients, whose fluctuations are assumed to be negligible such that $D_g(\boldsymbol{r},t) = D_{g,0}(\boldsymbol{r})$, $\forall(\boldsymbol{r},t)$. This assumption has shown to be valid in [29].

Since fluctuations are assumed to be very small, second-order terms on the form $\delta X(\boldsymbol{r},t) \cdot \delta Y(\boldsymbol{r},t)$ are neglected. The deviation of the time-dependent equations from the steady-state is then found by subtracting the time-independent equations, Eq. (2.13). Finally, a temporal Fourier-transform is applied, after which the following

first-order neutron noise balance equations in the frequency domain are obtained

$$\left[\nabla\cdot\begin{bmatrix}D_1(\boldsymbol{r}) & 0\\ 0 & D_2(\boldsymbol{r})\end{bmatrix}\nabla+\boldsymbol{\Sigma}_{dyn}(\boldsymbol{r},\omega)\right]\begin{bmatrix}\delta\phi_1(\boldsymbol{r},\omega)\\ \delta\phi_2(\boldsymbol{r},\omega)\end{bmatrix}=\begin{bmatrix}\delta\boldsymbol{S}_1(\boldsymbol{r},\omega)\\ \delta\boldsymbol{S}_2(\boldsymbol{r},\omega)\end{bmatrix} \tag{2.20}$$

where ω is the angular frequency of the perturbation [17, Eq. (3)]. The RHS of the above equation is a source vector corresponding to the studied scenario, which is expressed in terms of the perturbations to the macroscopic cross sections [17, eq. (4)]

$$\begin{bmatrix}\delta\boldsymbol{S}_1(\boldsymbol{r},\omega)\\ \delta\boldsymbol{S}_2(\boldsymbol{r},\omega)\end{bmatrix}=\boldsymbol{\phi}_r(\boldsymbol{r})\delta\Sigma_r(\boldsymbol{r},\omega)+\boldsymbol{\phi}_a(\boldsymbol{r})\begin{bmatrix}\delta\Sigma_{a,1}(\boldsymbol{r},\omega)\\ \delta\Sigma_{a,2}(\boldsymbol{r},\omega)\end{bmatrix}+\boldsymbol{\phi}_f(\boldsymbol{r},\omega)\begin{bmatrix}\delta\nu\Sigma_{f,1}(\boldsymbol{r},\omega)\\ \delta\nu\Sigma_{f,2}(\boldsymbol{r},\omega)\end{bmatrix} \tag{2.21}$$

Definitions of the matrices $\boldsymbol{\Sigma}_{dyn}, \boldsymbol{\phi}_a, \boldsymbol{\phi}_f$, and vector $\boldsymbol{\phi}_r$ in Eqs. (2.20–2.21) are found in Appendix A. The terms $\boldsymbol{\phi}_r, \boldsymbol{\phi}_a$, and $\boldsymbol{\phi}_f$ used to construct the noise source require the critical fluxes, which are obtained from solving the static equations in Eq. (2.13). The noise equation can also be written as

$$\mathcal{A}(\omega)\delta\boldsymbol{\phi}=\delta\boldsymbol{S}(\omega), \tag{2.22}$$

where $\mathcal{A}(\omega)$ denotes the frequency dependent noise operator.

2.3.2 Spatial and point-kinetic components

When studying neutron noise, it can be useful to distinguish between the point-kinetic component that is related to the global response of the reactor to a perturbation and the local, spatial component that is related to the specific characteristics of the perturbation. Following the flux factorisation approach commonly used in reactor kinetics [28], the time- and space-dependent neutron flux can be written as

$$\phi(\boldsymbol{r},t)=\underbrace{P(t)}_{\substack{\text{amplitude}\\ \text{factor}}}\underbrace{\psi(\boldsymbol{r},t)}_{\substack{\text{shape}\\ \text{function}}}, \tag{2.23}$$

where $P(t)$ is the amplitude of the flux, directly linked to the global reactor power, and $\psi(\boldsymbol{r},t)$ accounts for the spatial shape distribution of the flux. To examine small deviations around the steady-state, we utilise Eq. (2.18) and write

$$P(t)=P_0+\delta P(t),\qquad \psi(\boldsymbol{r},t)=\psi_0(\boldsymbol{r})+\delta\psi(\boldsymbol{r},t), \tag{2.24}$$

where P_0 is the amplitude and $\psi_0(\boldsymbol{r})$ the shape of the static flux. Inserting these into Eq. (2.23), discarding the second-order term, and subtracting the static flux $\phi_0(\boldsymbol{r})=P_0\psi_0(\boldsymbol{r})$ results in the following expression of the first-order noise

$$\delta\phi(\boldsymbol{r},t)=\underbrace{\phi_0(\boldsymbol{r})\frac{\delta P(t)}{P_0}}_{\substack{\text{point-kinetic}\\ \text{component}}}+\underbrace{P_0\delta\psi(\boldsymbol{r},t)}_{\substack{\text{spatial}\\ \text{component}}}. \tag{2.25}$$

The first term in Eq. (2.25) is referred to as the point-kinetic component and corresponds to fluctuations of the amplitude factor while retaining the shape of the

fundamental reactor mode (the static flux). This represents the global reactivity effect of the perturbation. The second term constitutes the spatial component and describes the perturbation of the flux shape, containing information about the position and spatial extent of the perturbation. In small systems and at low frequencies, the point-kinetic component typically dominates [28]. Although the spatial component is present, its contribution to detector signals may be comparatively small, which can obscure information related to the location of the perturbation.

The decomposition in Eq. (2.25) is not unique unless an additional constraint is imposed. This is done by requiring the spatial component to be orthogonal to the adjoint static flux

$$\left\langle \frac{1}{v}\boldsymbol{\phi}_0^\dagger, \delta\boldsymbol{\psi} \right\rangle = 0, \tag{2.26}$$

where $\boldsymbol{\phi}_0^\dagger$ denotes the adjoint static flux and $\langle \cdot, \cdot \rangle$ is an inner product, both formally presented in Section 2.4. This condition ensures that the spatial component contains no contribution from the fundamental reactor mode, such that all fluctuations of the static flux shape are represented by the point-kinetic term. Consequently, the relative perturbation to the flux amplitude can be written in the frequency domain as

$$\frac{\delta P(\omega)}{P_0} = \frac{\left\langle \frac{1}{v}\boldsymbol{\phi}_0^\dagger, \delta\boldsymbol{\phi} \right\rangle}{\left\langle \frac{1}{v}\boldsymbol{\phi}_0^\dagger, \boldsymbol{\phi}_0 \right\rangle}. \tag{2.27}$$

2.4 Adjoint neutron noise

The first-order noise equations in Eq. (2.20) describe the fluctuations in the neutron flux throughout the system. However, when comparing simulations to experimental data, the quantity of interest is not the full noise distribution, but rather the detector response at specific positions within the reactor. Adjoint theory provides a framework to efficiently compute quantities such as the neutron noise at selected detector locations without solving a new forward problem for each distinct noise source.

To define the adjoint problem we first need to specify an inner product. Denoting the complex conjugate with *, the inner product for two-group diffusion reads [27, Eq. (7-82)]

$$\langle f, g \rangle = \int \left[f_1^* g_1 + f_2^* g_2 \right] d\boldsymbol{r}. \tag{2.28}$$

Using the inner product we can then construct the adjoint operator $\mathcal{X}^\dagger$ to the operator $\mathcal{X}$ with [27, Eq. (7-83)]

$$\langle \mathcal{X}^\dagger f, g \rangle = \langle f, \mathcal{X} g \rangle. \tag{2.29}$$

With these definitions, we can write the associated adjoint formulations of the steady-state eigenvalue equation Eq. (2.16) and the first-order neutron noise equation Eq. (2.22) as

$$\mathcal{A}_0^\dagger \boldsymbol{\phi}_0^\dagger = \frac{1}{k_{\text{eff}}} \mathcal{F}^\dagger \boldsymbol{\phi}_0^\dagger \tag{2.30}$$

$$\mathcal{A}(\omega)^\dagger \delta\boldsymbol{\phi}^\dagger = \delta \boldsymbol{S}^\dagger, \tag{2.31}$$

where $\boldsymbol{\phi}_0^\dagger$ is the static adjoint flux, $\delta\boldsymbol{\phi}^\dagger$ the adjoint noise, and $\delta\boldsymbol{S}^\dagger$ an adjoint noise source. Physically, the adjoint flux can be interpreted as the importance neutrons at a given position and energy have to a specific quantity, such as the response of a detector.

To illustrate how the adjoint noise calculated in Eq. (2.31) can be used in the current context, we consider a generic reactor quantity Q defined as the weighted integral of the neutron flux. Then, the perturbation δQ is related to the forward neutron noise $\delta\phi$ via

$$\delta Q = \langle W, \delta\boldsymbol{\phi} \rangle, \tag{2.32}$$

where W is an arbitrary weighting function. From the basic definition of the adjoint operator given in Eq. (2.29), we can write the following identity

$$\langle \mathcal{A}^\dagger \delta\phi^\dagger, \delta\phi \rangle = \langle \delta\phi^\dagger, \mathcal{A}\delta\phi \rangle. \tag{2.33}$$

In the left- and right-hand sides of the above equation, we can substitute the adjoint noise Eq. (2.31) and the forward noise Eq. (2.22) respectively, and obtain the following expression

$$\langle \delta\boldsymbol{S}^\dagger, \delta\phi \rangle = \langle \delta\phi^\dagger, \delta\boldsymbol{S} \rangle. \tag{2.34}$$

By choosing the adjoint source $\delta\boldsymbol{S}^\dagger$ to be equal to the weighting function W, the left-hand side of Eq. (2.34) becomes identical to the definition of δQ in Eq. (2.32). Thus, the perturbation δQ can be evaluated directly using the adjoint neutron noise from Eq. (2.31) and the prescribed known noise source $\delta\boldsymbol{S}$, i.e.

$$\delta Q = \langle \delta\phi^\dagger, \delta\boldsymbol{S} \rangle. \tag{2.35}$$

In the specific case where δQ represents the neutron noise response of a thermal detector at position $\boldsymbol{r}_d$, we can select the suitable adjoint noise source as

$$\delta\boldsymbol{S}_d^\dagger(\boldsymbol{r}) = \begin{bmatrix} 0 \\ \delta(\boldsymbol{r} - \boldsymbol{r}_d) \end{bmatrix}, \tag{2.36}$$

where $\delta(\boldsymbol{r} - \boldsymbol{r}_d)$ is a Dirac-delta function centred at the position $\boldsymbol{r}_d$ of the detector [28]. Solving Eq. (2.31) with this noise source yields an adjoint noise field $\delta\boldsymbol{\phi}_d^\dagger$ corresponding to the sensitivity of the selected detector to perturbations throughout

the reactor, so that the noise at the detector position can be found from

$$\delta\boldsymbol{\phi}_d = \langle \delta\boldsymbol{\phi}_d^\dagger, \delta\boldsymbol{S} \rangle. \tag{2.37}$$

Another quantity of interest is the point-kinetic component introduced in Section 3.2.5. From Eq. (2.27), the perturbation to the flux amplitude δP can be interpreted as a quantity with the following adjoint noise source

$$\delta\boldsymbol{S}_\rho^\dagger = \frac{1}{v}\boldsymbol{\phi}_0^\dagger, \tag{2.38}$$

which requires the solution of the adjoint eigenvalue problem, Eq. (2.30). The resulting adjoint noise field $\delta\boldsymbol{\phi}_\rho^\dagger$ describes the sensitivity of the point-kinetic response to perturbations occurring throughout the reactor. Using Eq. (2.27), the relative perturbation to the flux amplitude can therefore be written in the adjoint approach as

$$\frac{\delta P(\omega)}{P_0} = \frac{\langle \delta\boldsymbol{\phi}_\rho^\dagger, \delta\boldsymbol{S} \rangle}{\left\langle \frac{1}{v}\boldsymbol{\phi}_0^\dagger, \boldsymbol{\phi}_0 \right\rangle}. \tag{2.39}$$

3

Methodology and simulation framework

In this chapter, we present the methodology of simulating and modelling the neutron noise experiments performed at the CROCUS reactor. The chapter is split into two parts. The first describes the experimental system itself, and the details surrounding the neutron noise experiments. The second part describes how the same system and experiments have been modelled and simulated using CORE SIM+.

3.1 Neutron noise experiments

In this section, the experimental work that lays the ground for our simulations will be presented. To begin with, the CROCUS reactor and its geometry is presented, followed by descriptions of the COLIBRI and POLLEN perturbation facilities that induce the neutron noise in the reactor. Then, a summary of the measurement campaigns and the experiments we model will be presented. Lastly, details surrounding the experimental data is discussed.

3.1.1 The CROCUS reactor

The structure of the CROCUS reactor is illustrated in Figure 3.1. The core is encased in a 1.2 cm thick aluminium vessel with a diameter of 130 cm. Light water circulates the core, serving as both a moderator and reflector. The active region of the reactor is nearly cylindrical with a height of 100 cm and a diameter of 60 cm. The core is divided into two connected fuel regions with fuel pins arranged in a square lattice. In the outer fuel region, 172 metallic uranium rods of enrichment 0.947 wt.% are distributed with a spacing of 2.917 cm between the rod centres. The inner fuel region consists of 336 uranium dioxide (UO_2) rods of enrichment 1.806 wt.%. The inner fuel rods are packed more tightly, with a spacing of 1.837 cm between rod centres. Due to the difference in centre-to-centre distances, a water filled gap between the two fuel regions is present. Two aluminium grid plates are placed on the top and bottom of the active region where they serve as anchor points for the fuel pins. The grid plates are coated in a 0.5 mm thick cadmium layer which reduces neutron leakage by absorbing escaping neutrons in the axial direction [12].

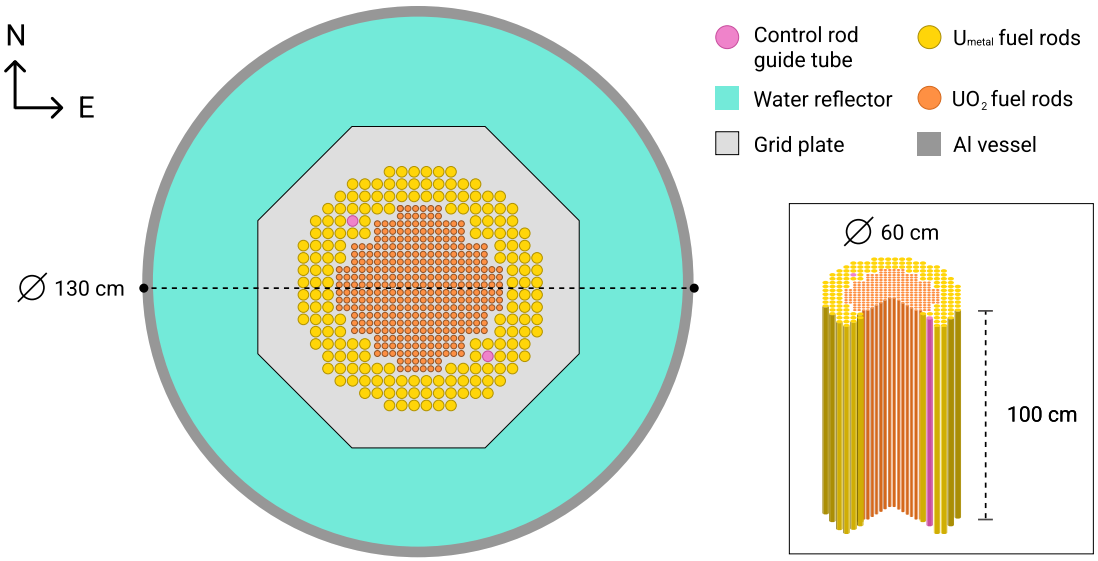

Figure 3.1: Illustration of the CROCUS reactor.

CROCUS operates at room temperature, where its temperature is managed using a multi-loop water system. The heat is initially transferred from the primary loop, i.e the water in the core, to a secondary circuit. It is then transferred to the third loop before its exhausted into the environment. The heat is transported between circuits via two heat exchangers. The reactor also uses an electrical heater to maintain a steady temperature. Criticality is controlled either by two boron carbide (B_4C) control rods or adjusting the level of the water covering the core.

3.1.2 The COLIBRI and POLLEN perturbation facilities

In the neutron noise experiments performed in the CROCUS reactor, two perturbation devices were used: the COLIBRI fuel rod oscillator, where COLIBRI stands for CROCUS Oscillator for Lateral Increase Between u-metal Rods and Inner zone, and the POLLEN vibrating absorber, standing for Pile Oscillator for Localized and Low Effect Noise [14].

The COLIBRI device is designed to emulate the oscillations of a fuel assembly with up to 18 fuel pins. It does so by mechanically vibrating the fuel pins using two moving plates located above and below the core grids, connected to an aluminium beam. The setup is schematically shown in Figure 3.2. A motor drives the oscillations, which generates sinusoidal fuel rod displacements that can be adjusted in both frequency and amplitude. The fuel rods oscillate laterally, i.e in the east-west direction. The POLLEN device is designed to emulate the axial vibrations of an absorber rod. The absorber is 7 mm in diameter, and consists of a 8.1 cm long, 1 mm thick cadmium sheet wrapped around a polymer rod. It is inserted into an aluminium guide tube with a diameter of 10 mm, positioned at the central axis of the core. The centre of the absorber rod has its nominal axial position at 80 cm above the bottom of the core. Unlike the COLIBRI fuel rod vibrations, the displacement of

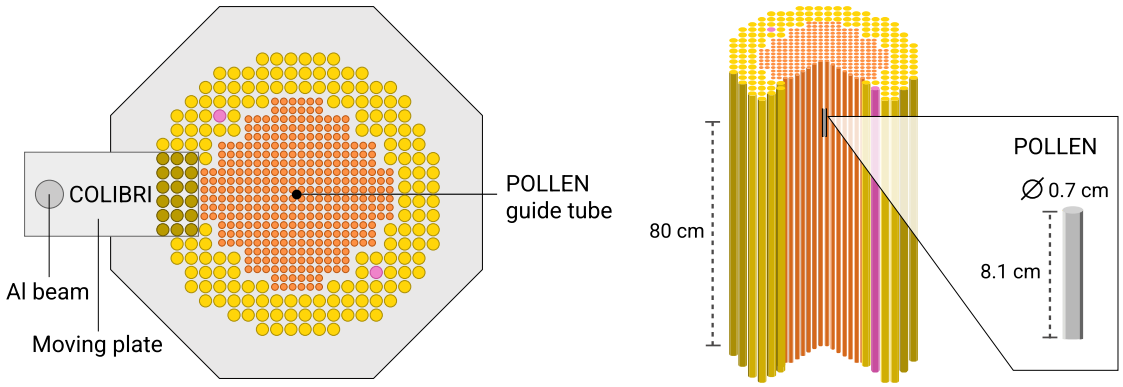

Figure 3.2: Schematic of the COLIBRI and POLLEN perturbation devices. The vibrating fuel rods are highlighted in a darker shade.

the POLLEN absorber rod was not pure sinusoidal. Instead, different asymmetrical displacement shapes were employed throughout the measurements. In this work, we consider only the experiments where the POLLEN displacement shape corresponds to the *mod 270* case described in the experimental report [14].

3.1.3 Description of measurement campaigns

In the context of the CORTEX-project, three measurement campaigns were carried out at the CROCUS reactor, where the experimental setup varied across the campaigns and individual measurements. These variations include (i) detector configuration, (ii) noise source specification, and (iii) operational parameters such as water level and number of control rods in operation. These differences are discussed below and summarised in Table 3.1.

In the first campaign, 11 neutron detectors were placed at in-core and ex-core positions. In subsequent campaigns, the number of detectors were increased to 15 and 18, respectively. Detectors of different types and models, with varying sizes and sensitive regions were used throughout the campaigns, with detailed specifications provided in the respective experimental reports [12], [13], [14]. All of the detectors are designed for detecting thermal neutrons, with the exception of detectors 9 and 10 in the second and third campaign which are sensitive to fast neutrons. Since this thesis focuses on thermal noise, detectors 9 and 10 were excluded from the analyses. The positions of all thermal detectors from each campaign are illustrated in Figure 3.3, and their exact coordinates are specified in Table B.1 of Appendix B. A small number of detector coordinates in the experimental documentation were found to be inconsistent with the physical detector locations shown in the detector maps or the descriptions found in text. These coordinates were therefore adjusted, and are indicated in the table. The first and second campaign included noise measurements using a COLIBRI noise source only, with the oscillatory frequency set to either 0.1 Hz or 1 Hz. In Campaign 1, the amplitude of the oscillations was set to 2 mm, and 1.5 mm in Campaign 2. In the third campaign, both COLIBRI and POLLEN devices were applied either separately or together. When applied together,

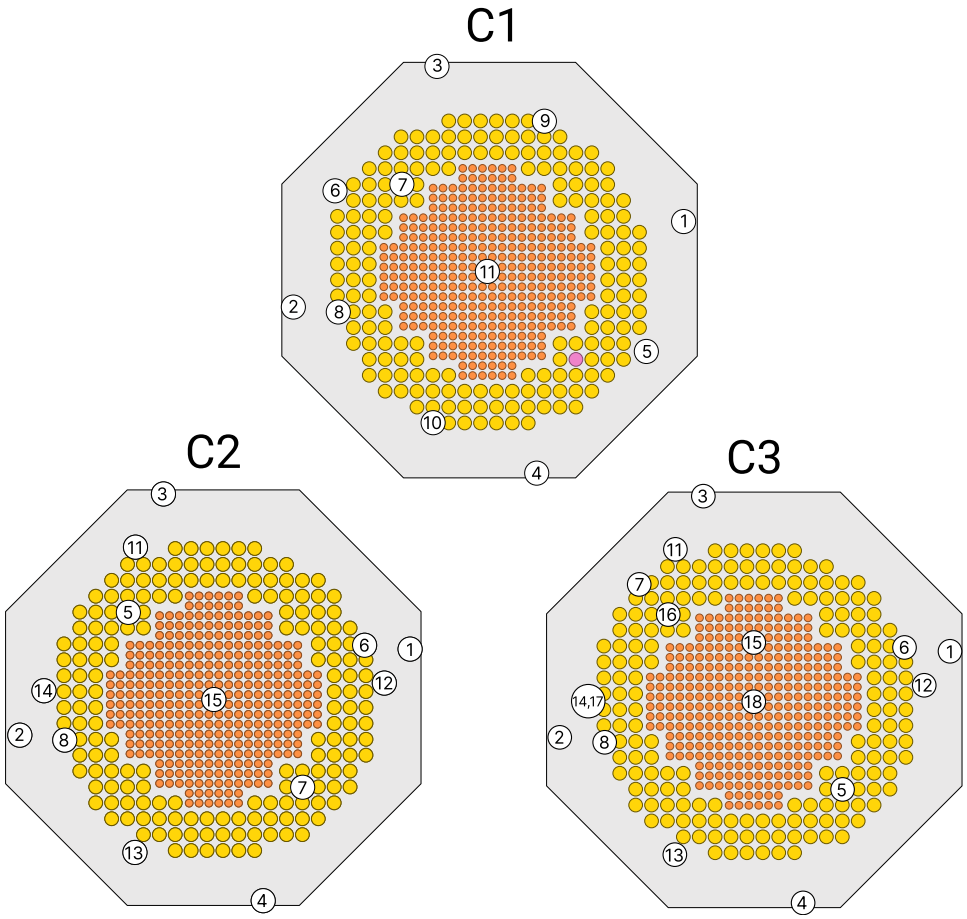

Figure 3.3: Map of thermal detectors in Campaign 1 (C1), Campaign 2 (C2), and Campaign 3 (C3).

the devices were set to oscillate in synchronisation. The purpose of this was for the oscillations of POLLEN to cancel, or at least reduce, the reactivity effect induced by COLIBRI, thus generating a noise signal with a more pronounced spatial dependence. In this campaign, both noise sources operated at 1 Hz, with the COLIBRI oscillation amplitude set to 1.5 mm.

CROCUS has two sites in which control rods can be inserted into guide tubes. In Campaign 1, the SE control rod was in operation while the NW guide tube was occupied by a detector. In subsequent campaigns, detectors were inserted in both the SE and NW guide tubes and the reactor was instead operated using the water level. The experimental report of Campaign 1 provides a fixed water level of 100 cm for all measurements, whereas in later campaigns the water level of each individual measurement is specified. Therefore, the water levels presented in Table 3.1 for Campaigns 2 and 3 correspond to the average water level across the measurements included in our analysis. The specific measurements modelled in our upcoming sections are specified in the table, using the same labels as in the experimental reports. Measurements beyond those listed in the table were performed which we did not have access to. Moreover, one of the combined COLIBRI-POLLEN measurements lacked data from one detector and was thus excluded from the analysis.

Table 3.1: Overview of the experimental campaigns.

	Campaign 1	**Campaign 2**	**Campaign 3**
Num. of Dets	11	13	16
Pert. Facility	COLIBRI	COLIBRI	COLIBRI, POLLEN
Frequency [Hz]	0.1, 1	0.1, 1	1
C. Amp. [cm]	0.2	0.15	0.15
P. shape	-	-	mod 270
Water Level [cm]	100	96.7	98.2
Control rods	SE	-	-
Exp. No.	12, 13	7, 8	C: 8, 10, 16, 27, 28 P: 21, 22, 25, 35, 36 C&P: 14, 17, 18, 20, 30, 37, 38

3.1.4 Definitions of quantities of interest

A fundamental quantity in neutron noise analysis is the relative noise associated with detector i, defined as [30, Eq. (1)]

$$\delta\phi_{\mathrm{rel},i}(\omega) = \frac{\delta\phi_i(\omega)}{\phi_{0,i}}. \tag{3.1}$$

Here, $\delta\phi_i$ is the noise at an angular frequency ω, and $\phi_{0,i}$ is the static flux at that location. This is a complex measure in the frequency domain where the amplitude and phase encode different physical effects, thus, its physical interpretation is not straightforward. A more convenient metric for comparing simulations and experiments are power spectrum densities (PSDs), which represent the noise power at a given frequency. The PSD can be evaluated at a single detector i, giving the auto power spectrum density (APSD_i), or between two detectors i and j, giving the cross power spectrum density ($\mathrm{CPSD}_{i,j}$). The $\mathrm{CPSD}_{i,j}$ is derived from the relative noise and computed as [30, Eq. (9)]

$$\mathrm{CPSD}_{i,j}(\omega) = \Big(\delta\phi_{\mathrm{rel},i}(\omega)\Big)\Big(\delta\phi_{\mathrm{rel},j}(\omega)\Big)^*, \tag{3.2}$$

where * denotes the complex conjugate. $\mathrm{CPSD}_{i,j}$ describes the correlation between two detectors, where a large value indicates strong correlation and that they respond to the same noise source. When $i = j$, we obtain the APSD_i, which quantifies the noise strength at a given frequency for that detector.

The experimental database provides the maximum likelihood estimates (MLEs) of the PSD amplitude and its phase, as well as the lower bound (LB) and upper bound

(UB) estimates corresponding to the 68.27 percentile boundaries. For any quantity X, the uncertainties were calculated from the MLE, UB, and LB according to

$$\sigma^{\mathrm{LB}} = X^{\mathrm{MLE}} - X^{\mathrm{LB}}, \qquad \sigma^{\mathrm{UB}} = X^{\mathrm{UB}} - X^{\mathrm{MLE}}. \tag{3.3}$$

The PSD amplitude and phase at the frequency of the perturbation are given both as direct values, and normalized with respect to a reference detector. In this work, we consider different quantities for the comparison between experiments and simulations depending on the campaign being analysed. These are discussed below.

Quantities of interest for Campaigns 1 and 2

For the analysis of Campaigns 1 and 2, PSD values are normalised with respect to a reference detector. This quantity has been used in previous studies, thus, using the same approach simplifies comparison between studies. The reference detector was selected as one far from the noise source, as it is less sensitive to the local effects of the perturbation. For Campaign 1, detector 5 was selected as a reference, whereas detector 12 was selected for Campaign 2. In general, the normalised PSD amplitude $A_{i,j}$ and phase $\theta_{i,j}$ for detector i with respect to a reference detector j is given as

$$A_{i,j} = \frac{|\mathrm{APSD}_i|}{|\mathrm{CPSD}_{i,j}|}, \qquad \theta_{i,j} = \arg(\mathrm{CPSD}_{i,j}). \tag{3.4}$$

These quantities were provided directly from the experimental campaigns, and can be interpreted as how much of the noise at detector i is local versus how much is shared with detector j. The corresponding lower and upper uncertainties $\sigma_{i,j}^{\mathrm{LB}}$ and $\sigma_{i,j}^{\mathrm{UB}}$ were calculated according to Eq. (3.3).

Quantities of interest for Campaign 3

In the analysis of Campaign 3, we consider the following quantity for each detector i:

$$\eta_i = \frac{|(\delta\phi_i)(\delta\phi_i)^*|}{\sum_d |(\delta\phi_d)(\delta\phi_d)^*|}. \tag{3.5}$$

This represents the fractional contribution of detector i to the total noise power across all detectors at the perturbation frequency. Since the experimental database provides the measured APSD values from the noise relative to the static flux, and no measured static flux is provided, we derive the experimental fractions as

$$\eta_{i,\mathrm{exp}} = \frac{|\mathrm{APSD}_i|\phi_{0,s,i}^2}{\sum_d |\mathrm{APSD}_d|\phi_{0,s,d}^2}, \tag{3.6}$$

where $\phi_{0,s,d}$ is the simulated static flux at the location of a generic detector d.

The corresponding uncertainties σ_i^{LB} and σ_i^{UB} were then calculated according to Eq. (3.3). When evaluating $\eta_{i,\mathrm{exp}}^{\mathrm{LB}}$ and $\eta_{i,\mathrm{exp}}^{\mathrm{UB}}$, the denominator in Eq. (3.6) was not recomputed for the LB and UB values. Instead, it was kept fixed at the value obtained using the MLEs.

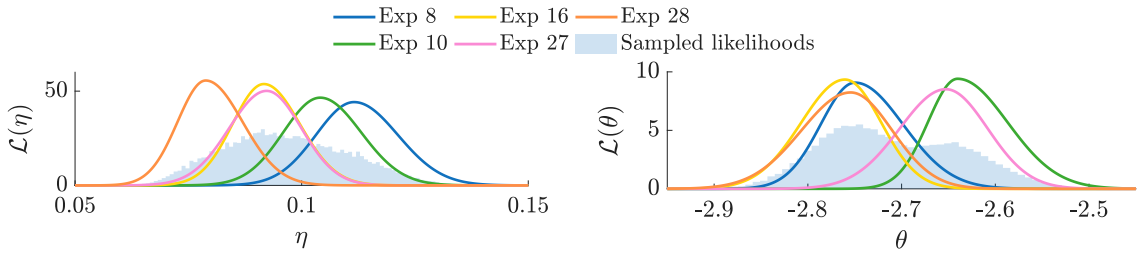

(a) **(b)**

Figure 3.4: Estimated likelihood distributions of (a): η and (b): θ for detector 17. The shaded regions represent the aggregated distributions.

The uncertainties and the noise power fractions $\eta_{i,\text{exp}}^{\text{MLE}}$ were used to generate approximate likelihood distributions of η for each detector and experiment. The likelihoods were modelled as asymmetric Gaussian with mean $\eta_{i,\text{exp}}^{\text{MLE}}$ and widths determined by σ_i^{LB} and σ_i^{UB}. The likelihoods were computed piecewise according to

$$\mathcal{L}_i(\eta) \propto \begin{cases} \exp\left(-\frac{1}{2}\frac{(\eta-\eta_{i,\text{exp}}^{\text{MLE}})^2}{\sigma_{i,\text{LB}}^2}\right), & \eta \leq \eta_{i,\text{exp}}^{\text{MLE}}, \\ \exp\left(-\frac{1}{2}\frac{(\eta-\eta_{i,\text{exp}}^{\text{MLE}})^2}{\sigma_{i,\text{UB}}^2}\right), & \eta > \eta_{i,\text{exp}}^{\text{MLE}}. \end{cases} \tag{3.7}$$

Each individual likelihood was then sampled, and the samples were combined into a single aggregated distribution per detector. The final distributions were visualised in histograms, as exemplified in Figure 3.4a for detector 17 from the COLIBRI experiments.

For the analysis of the phase in Campaign 3, we select a reference detector following the same approach as in the other campaigns. Specifically, we calculate the phase with respect to detector 12 according to Eq. (3.4). Similarly to the noise power fraction η, estimated likelihood functions were generated for the phase θ and the individual likelihood functions were sampled and combined into a single distribution per detector (see Figure 3.4b). The likelihood functions were estimated using an asymmetric circular model inspired by the von Mises distribution [31, p. 36]:

$$\mathcal{L}_i(\theta) \propto \exp\left(\kappa(\theta)\cos(\theta-\theta_i^{\text{MLE}})\right). \tag{3.8}$$

Here, the parameter κ determines the width of the function and can be seen as an analogue to $1/\sigma^2$ of the normal distribution. To preserve the asymmetry of the measured bounds, κ was approximated and defined piecewise from the measurement uncertainties σ_i^{LB} and σ_i^{UB} (calculated using Eq. (3.3)) according to

$$\kappa(\theta) = \begin{cases} 1/(\sigma_i^{\text{LB}})^2, & \theta \leq \theta_i^{\text{MLE}} \\ 1/(\sigma_i^{\text{UB}})^2, & \theta > \theta_i^{\text{MLE}}. \end{cases} \tag{3.9}$$

3.2 Modelling and simulations in CORE SIM+

In this section we present the simulations of the CROCUS experiments performed in CORE SIM+. To begin with, the computational workflow to obtain neutron noise solutions using both a direct and adjoint approach is outlined. After this, the spatial discretisation and modelling of the CROCUS reactor is presented, followed by the construction of neutron noise sources. This includes the description of both COLIBRI and POLLEN-like noise sources. Finally, the simulated cases considered in this work are summarised.

3.2.1 Numerical solvers

CORE SIM+ is equipped with multiple solvers that are used in different steps of the simulation workflow. The first solver corresponds to the forward eigenvalue problem where the static equation (2.16) is solved numerically to determine the effective multiplication factor and static flux of the system. After discretisation, the same equation can be expressed on matrix form as

$$\boldsymbol{A}_0 \, \boldsymbol{\Phi}_0 = \frac{1}{k_{\text{eff}}} \boldsymbol{F} \, \boldsymbol{\Phi}_0. \tag{3.10}$$

The second solver calculates the neutron noise in the frequency domain given a neutron noise source in a critical reactor. This corresponds to solving the first-order neutron noise equation (2.22), or similarly on matrix form

$$\boldsymbol{A}(\omega) \, \delta\boldsymbol{\Phi} = \delta\boldsymbol{S}. \tag{3.11}$$

The third solver is an adjoint eigenvalue solver which obtains the adjoint static flux and effective multiplication factor by numerically solving the adjoint static equation (2.30), or

$$\boldsymbol{A}_0^\dagger \, \boldsymbol{\Phi}_0^\dagger = \frac{1}{k_{\text{eff}}} \boldsymbol{F}^\dagger \, \boldsymbol{\Phi}_0^\dagger. \tag{3.12}$$

In addition to the above solvers, CORE SIM+ was equipped with an additional solver following recent developments. This fourth solver computes the adjoint neutron noise from Eq. (2.31), which can be expressed on matrix form as

$$\boldsymbol{A}^\dagger(\omega) \, \delta\boldsymbol{\Phi}^\dagger = \delta\boldsymbol{S}^\dagger. \tag{3.13}$$

Together, these four solvers constitute the basis for performing simulations of the CROCUS neutron noise experiments.

3.2.2 Simulation workflow

For all simulations, the workflow begins with defining the spatial discretisation and geometry of the reactor. This sets the computational mesh used during simulations and defines the spatial volumes over which the reactor quantities are averaged. The spatial discretisation implemented in this work, along with the cross section

distributions used for modelling the CROCUS reactor is described in Section 3.2.3. The simulation procedure then consists of three main steps: (i) solution of the static eigenvalue problem, (ii) construction of noise sources, and (iii) computation of the frequency-domain neutron noise, using either a direct or adjoint approach. The two approaches are illustrated in Figure 3.5.

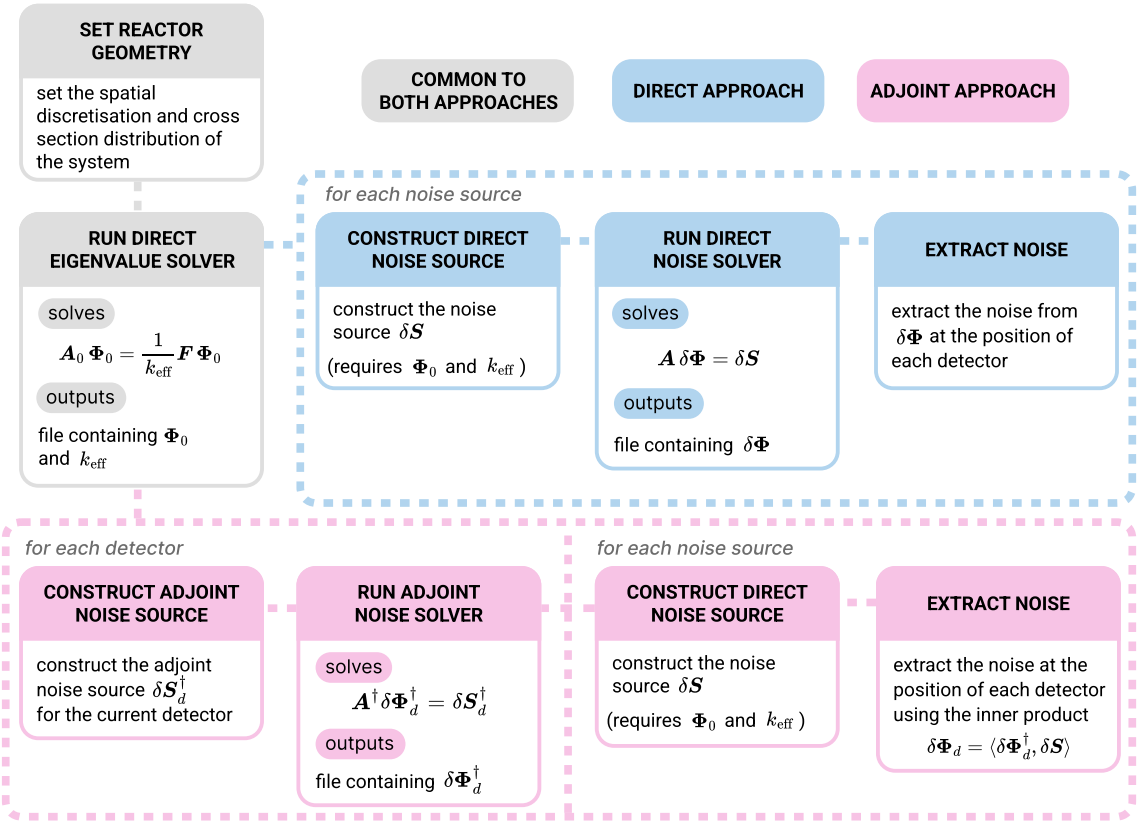

Figure 3.5: Overview of the direct and adjoint approaches for simulating the first-order neutron noise using CORE SIM+.

In the direct (or forward) approach the spatial noise distribution induced by a chosen noise source is computed throughout the reactor. This begins by solving the critical eigenvalue equation and obtaining the static flux, which is necessary for the construction of noise sources. After the neutron noise spatial distribution is calculated, the neutron noise values at the location of the detector volumes are extracted.

In the adjoint approach, adjoint sources corresponding to each detector are defined and their adjoint noise spatial distributions are obtained from the adjoint noise solver. The first-order neutron noise at the position of each detector can then be found from the simple inner product shown in Eq. (2.37). As such, the adjoint approach offers an advantage to quickly calculate the neutron noise at the detector positions, without having to rerun the noise solver for each source. However, unlike the direct method the full distribution of the neutron noise is not obtained.

3.2.3 Reactor models and numerical mesh

In CORE SIM+, the spatial discretisation of the system is defined by specifying the dimension of computational nodes in the x- y- and z-directions, which are then assigned macroscopic cross sections and diffusion coefficients [17]. The reactor models used in this work are based on a previous CORE SIM+ model developed within the CORTEX project and used for the analysis of Campaigns 1 and 2 [30]. This model was then modified to fit the needs of this work. The models of the three experimental campaigns are set apart by (i) the use of two-dimensional (2D) or three-dimensional (3D) geometries, (ii) the refinement of the computational mesh, (iii) the inclusion of POLLEN in Campaign 3, (iv) the modelling of the average water level, and (v) the positioning of the detectors. These differences are summarised in Table 3.2 and discussed below. To illustrate the differences between the models, Figure 3.6 shows a model used for Campaign 3, including the distribution of homogenised media.

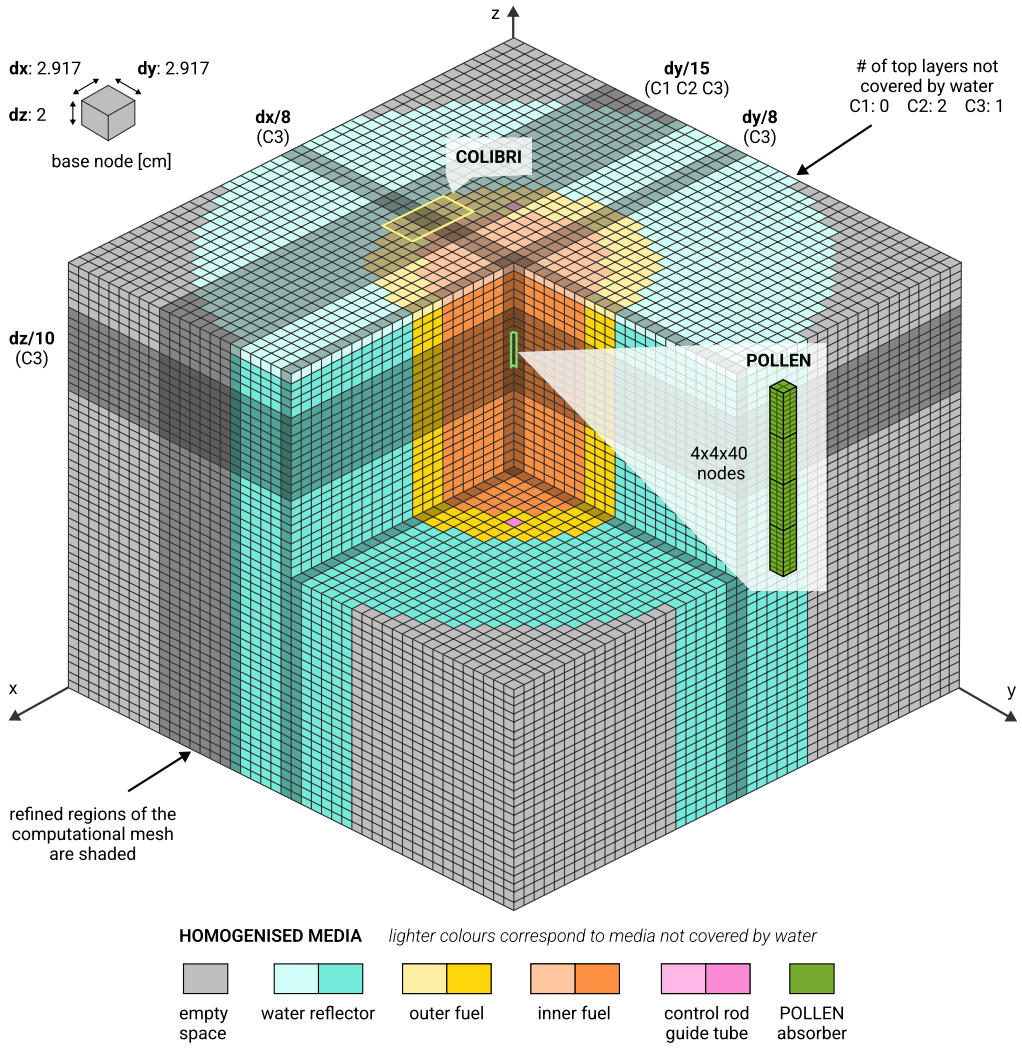

Figure 3.6: Three-dimensional model of the CROCUS reactor, corresponding to Campaign 3. The colour of the nodes indicate the different types of media, where lighter shades represents media not covered by water. Regions with additional refinement are shaded. A cutout is shown to illustrate the position of the POLLEN absorber.

For simulations of Campaigns 1 and 2, in which exclusively included the COLIBRI perturbation that moves uniformly along the z-direction, 2D models were employed. The base 2D model consist of a 44×44 grid of nodes with lateral dimensions of 2.917 cm, set with values of macroscopic fission and absorption cross sections in the fast and thermal groups, as well as removal cross sections and diffusion coefficients corresponding to the various media of the CROCUS reactor. To verify that no relevant physical details were lost when simulating the experiments in 2D, and to simulate experiments of the axially vibrating POLLEN-absorber in Campaign 3, corresponding 3D models were also constructed. These were obtained by stacking 50 axial layers, identical to the 2D models and each with a height of 2 cm, on top of each other.

CORE SIM+ allows for the computational mesh to be given finer resolutions in regions where the spatial gradient of the flux is strong, for instance in the vicinity of perturbations. For this reason, models of the three experimental campaigns were given different refinements depending on the perturbations that were present. In the case of COLIBRI, meshes were refined in the y-direction around the perturbation. In models of Campaign 3, refinement around POLLEN in the z-direction was added, along with some lateral refinement to make computational nodes match the physical dimensions of the small POLLEN absorber. When simulating experiments with POLLEN, a $4 \times 4 \times 40$ sized region of nodes was updated with new macroscopic cross sections. These cross sections were generated using a Monte Carlo approach. Considering the small size of the absorber, an accurate estimate of the cross sections would require expensive calculations. Therefore, a simplified 2D model of the core including the absorber was used to determine a less time-consuming (although rough) estimate that could be used as a starting point of the current study.

To model the water level across campaigns, the average water levels were approximated to the closest number of axial layers. The macroscopic cross sections of the same number of layers at the top of the 3D models were then set to ones representing the core not covered by water. Finally, the detector positions shown in Figure 3.3 and Appendix B were mapped to their closest computational nodes in the unrefined meshes, keeping detector volumes to the same size. The detector locations in the computational meshes are shown in Figure 3.7.

Table 3.2: Summary of the employed CORE SIM+ reactor models, highlighting differences in mesh refinement, POLLEN modelling, and water-level treatment.

Campaign	Model	2D/3D	Top Layers	COLIBRI Ref.	POLLEN Ref.	POLLEN Cross Sec.
C1	A1	2D	-	x	-	-
	B1	3D	0	x	-	-
C2	A2	2D	-	x	-	-
	B2	3D	2	x	-	-
C3	A3	3D	1	x	x	-
	B3	3D	1	x	x	x

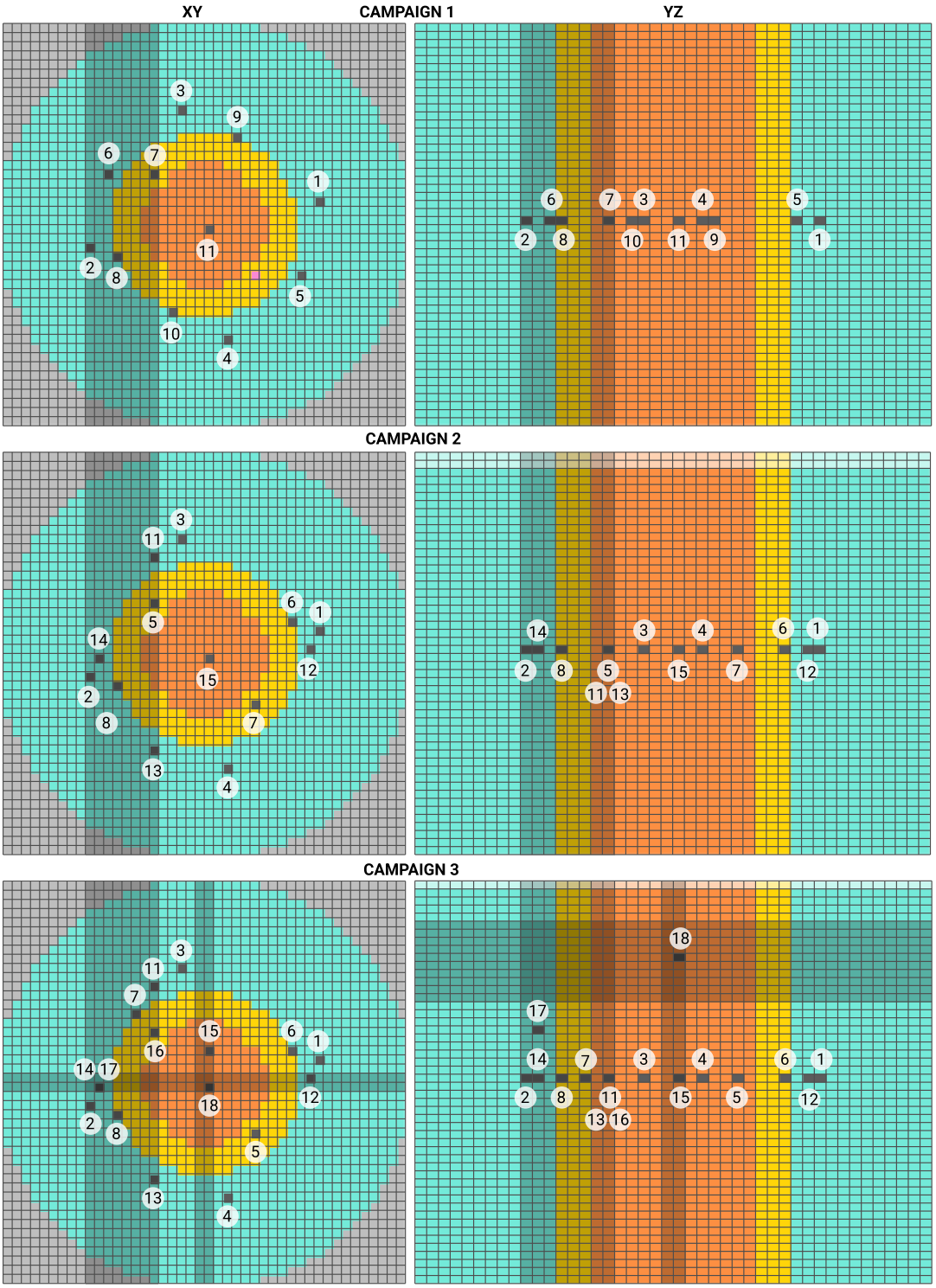

Figure 3.7: Location of detector volumes in the computational meshes, projected onto the mid-elevation XY-plane and a YZ-plane crossing the centre of the core.

3.2.4 Construction of direct and adjoint noise sources

The construction of noise sources consists of two types: (i) the modelling of direct noise sources, corresponding to the studied perturbations, and (ii) the construction of adjoint noise sources. The two types and their applications to this work are described below. In addition to this, the construction of POLLEN-like noise sources is presented in Section 3.2.5.

Direct noise sources

Direct noise sources are expressed using Eq. (2.21), which depends on the perturbations to the macroscopic cross sections. The modelling of these perturbations in turn depends on the characteristics of the noise source. In this work, the ϵ/d-model [32] is used to describe the vibrations of the COLIBRI and POLLEN facilities.

The model expresses vibrations as Dirac-like perturbations at the boundary between the moving region and its surroundings. The perturbation to some macroscopic cross section of type α belonging to energy group g due to a vibration in the x-direction is then expressed as

$$\delta\Sigma^x_{\alpha,g}(\boldsymbol{r},\omega) = \gamma^x_\alpha \cdot \delta(x - x_{b1}) \left[\Sigma^{lob1}_{\alpha,g} - \Sigma^{rob1}_{\alpha,g}\right] + \gamma^x_{\alpha,g} \cdot \delta(x - x_{b2}) \left[\Sigma^{lob2}_{\alpha,g} - \Sigma^{rob2}_{\alpha,g}\right] \quad (3.14)$$

where x_{b1} and x_{b2} are the locations of the first and second boundary to the left and right of the vibrating region. In turn, $\Sigma^{lob}_{\alpha,g}$ and $\Sigma^{rob}_{\alpha,g}$ are the macroscopic cross sections to the left and right of the respective boundaries. The constant γ^x_α is the intensity of the vibrations, equivalent to the total displacement in x.

Numerically, the Dirac-deltas at each of the boundaries are approximated as

$$\delta(x - x_b) \approx \begin{cases} \dfrac{1}{\Delta x} & \text{in nodes on either side of the boundary} \\ 0 & \text{otherwise} \end{cases} \quad (3.15)$$

where Δx is the combined length of the nodes on both sides of the boundary, in the direction of the perturbation.

In this manner, perturbations to the macroscopic cross sections due to the COLIBRI (vibrating in the y-direction), and POLLEN (vibrating in the z-direction) facilities were modelled and the corresponding noise sources constructed. The location of both sources are shown in Figure 3.8, and the parameters that were used to construct the noise sources are summarised in Section 3.2.6.

In the COLIBRI case, sources were modelled as perturbations to all cross sections, with varying frequencies and intensities depending on the experiments being simulated. As mentioned in Section 3.2.3, the cross sections of the POLLEN absorber are approximations that do not fully describe the physics, and thus contributes to the accuracy of the source models. For this reason, some different options of modelling a POLLEN-like noise source were tested, detailed in Section 3.2.5.

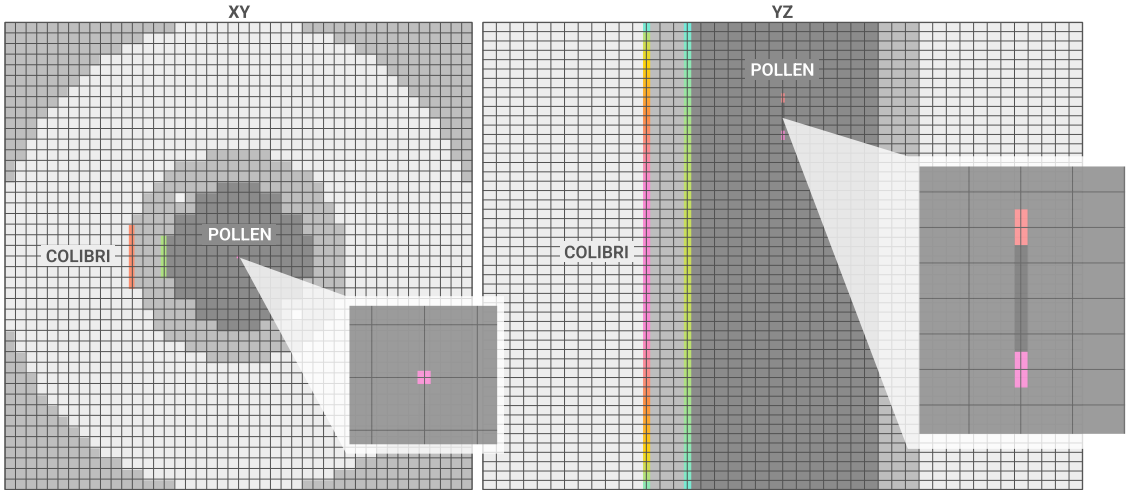

Figure 3.8: Example of direct noise sources corresponding to COLIBRI and a POLLEN-like noise source, showing their locations in the XY- and YZ-plane. The XY-slice sits at the bottom node of the POLLEN absorber, and the YZ-slice runs though the centre of the core. For visibility, the noise sources have been constructed over four nodes on either side of the boundary, instead of just one, i.e. quadrupled in width.

Adjoint noise sources

As shown in Eq. (2.36), the adjoint noise source $\delta \boldsymbol{S}_d^\dagger$ associated with a detector is given by a Dirac-delta function at the centre of the detector position $\boldsymbol{r_d}$. The Dirac-delta is numerically approximated as

$$\delta(\boldsymbol{r} - \boldsymbol{r_d}) \approx \begin{cases} \dfrac{1}{V_d} & \text{in nodes constituting the detector volume} \\ 0 & \text{otherwise} \end{cases} \tag{3.16}$$

where V_d is the volume of the detector in the numerical mesh. In addition to this, an adjoint noise source which can be used to compute the perturbation to the reactor power in the thermal group is given by

$$\delta \boldsymbol{S}_\rho^\dagger = \begin{bmatrix} 0 \\ \dfrac{1}{v_2} \phi_{0,2}^\dagger \end{bmatrix} \tag{3.17}$$

where $\phi_{0,2}^\dagger$ is the thermal adjoint static flux of the reactor.

With the above definitions, adjoint noise sources of each of the thermal detectors were constructed for each reactor model. For Campaign 3, an adjoint source corresponding to the perturbation of the reactor power was also constructed, which is used to investigate the point-kinetic component of the noise.

3.2.5 Construction of POLLEN-like noise sources

Considering the approximated macroscopic cross sections used in this work, it is not possible to construct a fully accurate model of POLLEN. However, it is possible to construct POLLEN-like noise sources that model an axially vibrating absorber moving at the same location and with the same displacement as the POLLEN perturbation. Although not fully realistic, it offers a way to study the induced neutron noise and compare the simulations to experimental data.

Since the motion of POLLEN is not perfectly sinusoidal [14, Fig. 16], the amplitude of the perturbation was found by decomposing the movements of POLLEN into its first five Fourier harmonics. The amplitude of the first harmonic, approximately 1.06 cm, which corresponds to 1 Hz, was then used when defining noise sources. Due to its thermally absorptive nature, the POLLEN-like noise sources were modelled as perturbations to the thermal absorption cross section only.

To begin with, two POLLEN-like sources were constructed using Eq. (3.14), one in which the cross section difference between the absorber and the surroundings was small, and one in which it was larger. In the first case, the difference was taken with respect to the absorber and the cross sections corresponding to the inner fuel surrounding the absorber. This produced a relatively weak source, since the cross sections that were used for the POLLEN absorber lie close to the inner fuel. In the second case, the difference between the absorber and the cross sections of the reflector was instead considered. This resulted in a stronger noise source, on the same scale as the COLIBRI source. These two models are from here on referred to as the fuel-referenced and reflector-referenced models of the POLLEN perturbation.

Cancelling the point-kinetic component of the noise

In addition to the ones above, a third POLLEN-like source was also investigated. As described in Section 2.3.2, the noise is a superposition of a point-kinetic component, which carries information about the global reactivity effect of the perturbation, and a spatial component which contains information about its location. One of the ideas behind implementing the POLLEN source in Campaign 3 was to enhance the spatial component of the noise [14], effectively making the point-kinetic components of COLIBRI and POLLEN cancel each other. For this reason, we investigated the modelling of a POLLEN-like absorber and its effect on reducing the point-kinetic noise component induced by COLIBRI. This was done in the following way.

Under the assumption that linear theory holds, the neutron noise induced by two perturbations is equal to the sum of the neutron noise induced by the separate perturbations. Using Eq. (2.25), the noise distribution $\delta\phi^{\mathrm{C}}$ induced by COLIBRI and $\delta\phi^{\mathrm{P}}$ induced by a POLLEN-like noise source can be written as

$$\begin{aligned}\delta\phi &= \delta\phi^{\mathrm{C}} + \delta\phi^{\mathrm{P}} \\ &= \underbrace{P_0\left[\delta\psi^{\mathrm{C}} + \delta\psi^{\mathrm{P}}\right]}_{\text{Spatial component}} + \underbrace{\phi_0\left[\frac{\delta P^{\mathrm{C}}}{P_0} + \frac{\delta P^{\mathrm{P}}}{P_0}\right]}_{\text{Point-kinetic component}} .\end{aligned} \tag{3.18}$$

The idea is to find a scaling factor γ^{PKC} that rescales the intensity of the POLLEN-like source so that the point kinetic-component in Eq. (3.18) vanishes. This is expressed as

$$\begin{aligned} 0 =& \frac{\delta P^{\mathrm{C}}}{P_0} + \gamma^{\mathrm{PKC}} \frac{\delta P^{\mathrm{P}}}{P_0} \\ \Rightarrow \quad \gamma^{\mathrm{PKC}} =& -\frac{\delta P^{\mathrm{C}}}{P_0} \Big/ \frac{\delta P^{\mathrm{P}}}{P_0} . \end{aligned} \tag{3.19}$$

The scaling factor γ^{PKC} can be determined through either the direct or the adjoint approach. The direct approach relies on Eq. (2.27), which leads to

$$\gamma_d^{\mathrm{PKC}} = -\frac{\left\langle \frac{1}{v}\phi_0^\dagger, \delta\phi^{\mathrm{C}} \right\rangle}{\left\langle \frac{1}{v}\phi_0^\dagger, \delta\phi^{\mathrm{P}} \right\rangle} \tag{3.20}$$

and the adjoint approach makes use of Eq. (2.39) which results in

$$\gamma_a^{\mathrm{PKC}} = -\frac{\left\langle \phi_\rho^\dagger, \delta S^{\mathrm{C}} \right\rangle}{\left\langle \phi_\rho^\dagger, \delta S^{\mathrm{P}} \right\rangle}. \tag{3.21}$$

Using the above formulations, the scaling factors γ_d^{PKC} and γ_a^{PKC} were evaluated for a source pair corresponding to a COLIBRI source and a POLLEN-like source. The two methods yielded approximately the same scaling factor, which was then used to construct a new rescaled POLLEN-like source.

3.2.6 Simulated cases

For each reactor model, static simulations were performed to obtain the unperturbed flux distributions of the systems. An example of the static thermal flux is shown in Figure 3.9. For the B3 model of Campaign 3, an adjoint static flux was also computed to enable the point-kinetic analysis described in Section 3.2.5. Direct and adjoint noise simulations were then carried out using the source definitions described in Section 3.2.4, corresponding to the various experiments. An overview of the simulated cases is presented in Table 3.3.

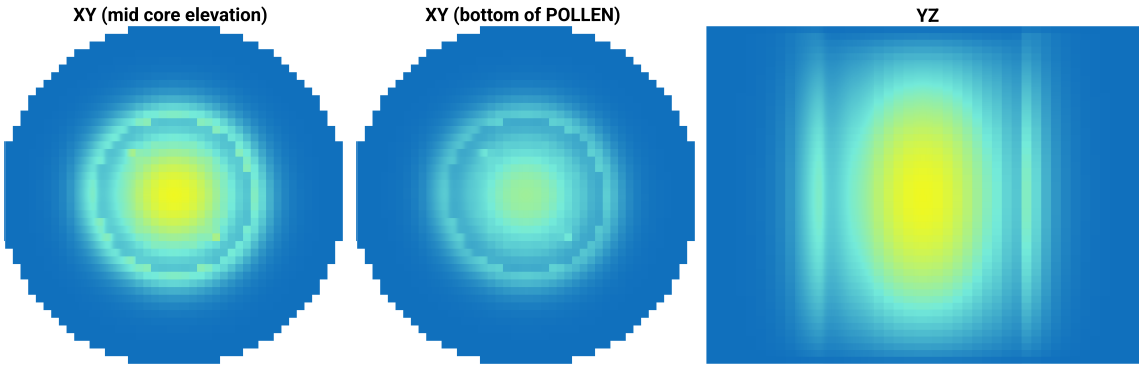

Figure 3.9: Thermal static flux distribution in the B3 model of Campaign 3. The XY-slices sit at mid-core elevation, and at the elevation of POLLEN's lower boundary. The YZ-slice runs through the centre of the core.

Table 3.3: Overview of simulated cases.

Camp.	Pert. Fac.	Model	f [Hz]	γ [cm]	$\delta\Sigma_\alpha$	Exp. No.
C1	COLIBRI	A1	0.1	0.2	all	12
		B1	0.1	0.2	all	
	COLIBRI	A1	1	0.2	all	13
		B1	1	0.2	all	
C2	COLIBRI	A2	0.1	0.15	all	7
		B2	0.1	0.15	all	
	COLIBRI	A2	1	0.15	all	8
		B2	1	0.15	all	
C3	COLIBRI	A3	1	0.15	all	8, 10,
		B3	1	0.15	all	16, 27, 28
	POLLEN	B3	1	1.06	$\delta\Sigma_{a,2}$	21, 22,
		B3	1	1.06	$\delta\Sigma_{a,2}$ *	25, 35, 36
			C	**P**	**C** **P**	
	COLIBRI & POLLEN	B3	1	0.15	1.06	all $\delta\Sigma_{a,2}$ *	14, 17, 18
		B3	1	0.15	$1.06 \cdot (-977)$	all $\delta\Sigma_{a,2}$	20, 30, 37, 38

* Constructed using macroscopic cross section values of the reflector, instead of the inner fuel surrounding the POLLEN absorber.

4

Results and discussion

In this chapter we present the results of the neutron noise simulations. Section 4.1 covers the first and second experimental campaigns where the simulated noise is compared to experimental data. Since these campaigns have been analysed previously [17], [19], [20], this serves mainly as a verification that (i) the direct and adjoint approaches yield similar results, (ii) the 2D and 3D models for COLIBRI give equivalent outcomes, and (iii) the results are consistent with previous CORE SIM+ simulations of the same experiments.

Section 4.2 presents the results of the third campaign which has not previously been analysed with CORE SIM+. Beginning with an analysis of the noise distributions produced by the three investigated neutron noise source configurations, followed by a comparison against experimental detector responses.

4.1 Simulations of Campaigns 1 and 2

For Campaigns 1 and 2, simulations were performed with COLIBRI oscillating at 0.1 Hz, corresponding to experiments 12 (C1) and 7 (C2), and at 1 Hz, corresponding to experiments 13 (C1) and 8 (C2). In all four cases, simulations were made using both 2D and 3D models of the CROCUS reactor, presented in Section 3.2.3, as well as using the direct and adjoint approaches described in Section 3.2.2. We compare the results from the simulations and the experimentally measured detector responses via the quantities defined in Eq. (3.4), taken according to the detector configurations discussed in Section 3.1.3 and shown in the numerical meshes in Figure 3.7.

The results are presented in Figure 4.1, which shows the relative noise and phase with respect to reference detectors 5 and 12 for Campaigns 1 and 2, respectively. Detectors 3–10 are shown for Campaign 1, which are the same as presented in [19]. The figures of Campaign 2 include detectors 1–15, excluding the non-thermal detectors 9 and 10. For each of the simulated cases, the results are almost identical regardless of whether a direct or adjoint approach was used, or whether the system was modelled in 2D or 3D. In addition to this, the simulated values align well to previous simulations performed with CORE SIM+, which are summarised in [20].

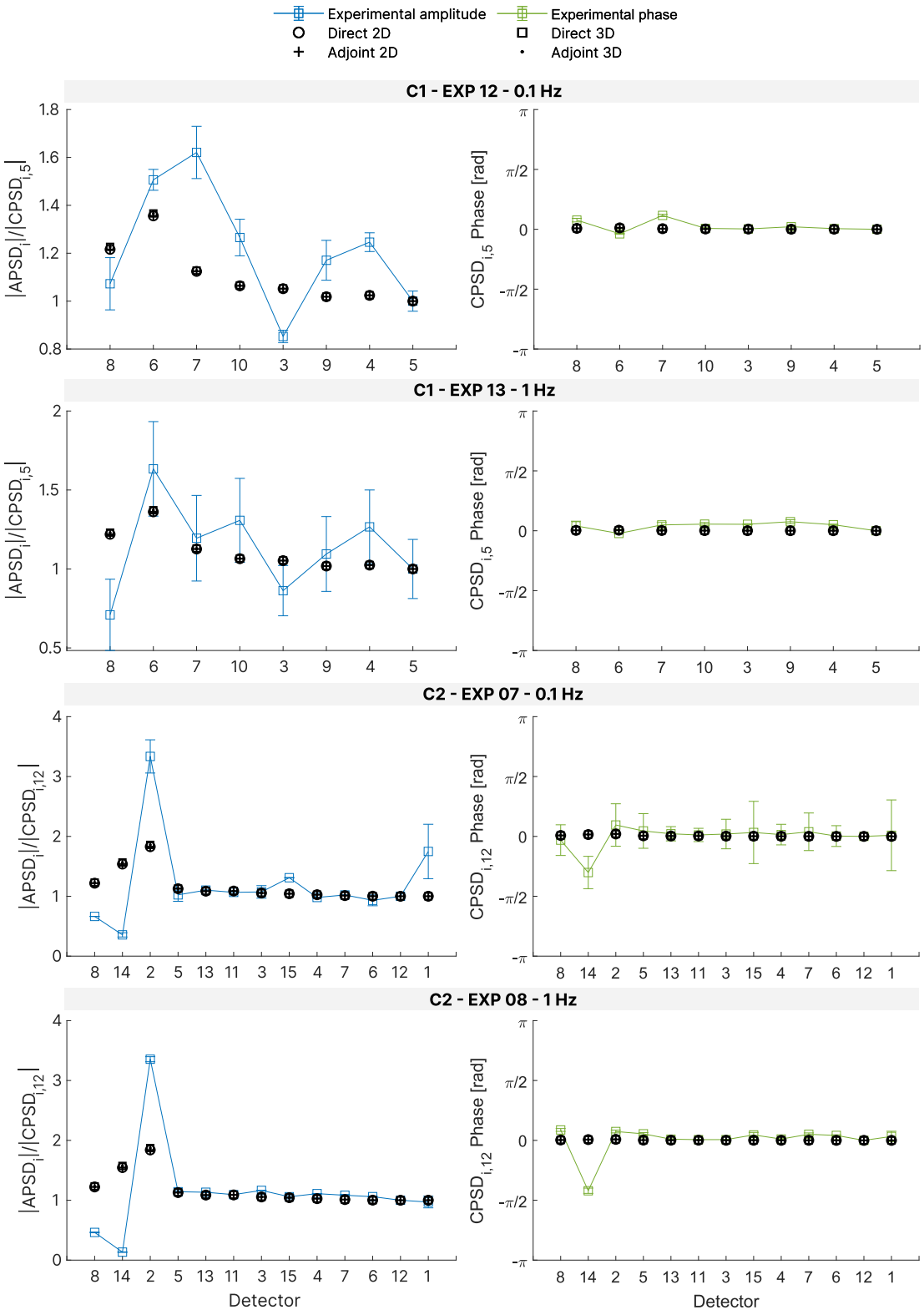

Figure 4.1: Relative noise amplitude and phase of experiments from the 1st and 2nd experimental campaign. From the top: experiments 12 and 13 from Campaign 1, with detector 5 as reference. Followed by experiments 7 and 8 from Campaign 2, with detector 12 as reference. The uncertainty range of the experimental data correspond to $\pm 1\sigma$. The detectors are ordered by distance to the COLIBRI perturbation, from closest to farthest.

In the Campaign 1 case, the simulated relative CPSD values of experiment 12 show no overlap with experimental data. The simulations agree much better with experiment 13, in which predictions of detectors 6, 7, 10, 9, and 5 fall within the uncertainty range, and detectors 3 and 4 just outside of it. For Campaign 2, the simulated values of detector 5 and onward are almost constant. This is thought to stem from the highly point-kinetic response of the reactor, meaning spatial noise information is present only in the close vicinity of the perturbation. The point-kinetic component of the noise is proportional to the static flux, which results in the constant behaviour when the detector responses are all normalized with respect to the static flux. The experiments follow the same trend, except for detectors 15 and 1 in experiment 7 which deviate from this behaviour. For detectors close to the source (8, 14, and 2), the simulations fail to predict the experimental data, most likely due to the diffusion approximation not holding up, and failing to resolve the steep spatial changes in the flux.

In all simulated cases, the relative phase is simulated to be approximately zero across all detectors. In the experimental data, there seems to exist some phase information which is not present in the simulations, mainly the dip at detector 14, which is present in both experiments 7 and 8.

4.2 Simulations of Campaign 3

Campaign 3 includes experiments in which COLIBRI and POLLEN were applied both separately and simultaneously. The experiments were simulated using a 3D geometry, and three different ways of modelling the POLLEN-like source were explored. In this section, we first investigate the spatial distribution of the absolute and relative thermal neutron noise induced by the perturbations, considering only the results from the direct simulations. We then compare the simulated responses at the detector volumes obtained from both the direct and joint approaches with the corresponding experimental measurements.

4.2.1 Neutron noise distribution induced by COLIBRI

We first consider the experiments with COLIBRI oscillating at a frequency of 1 Hz and examine the spatial distribution of the simulated thermal noise amplitude. By taking the XY plane at mid-core elevation (first row of Figure 4.2), we see that the noise closely follows the shape of the static flux (Figure 3.9) in regions away from the source. In these regions, the relative noise amplitude is nearly constant, indicating that spatial effects induced by COLIBRI vanish and the response approaches a point-kinetic behaviour. However, near the source the spatial component of the noise becomes more significant. Strong local gradients in both the noise and relative noise appear, with prominent features that coincide with the source boundaries. The distributions of the static flux and neutron noise along the y-direction are shown in the third row of Figure 4.2. These profiles further demonstrate that the COLIBRI-induced noise is dominated by the point kinetic component farther from the source, while the spatial component gains significance closer to the source.

We examine an axial YZ slice at the core centre along the x-direction (second row of Figure 4.2) and observe that the shapes of the static flux (Figure 3.9) and the COLIBRI-induced noise closely match, resulting in a relative noise that is approximately uniform along z. This is also evident in the static-flux and noise distributions along the z-direction (fourth row), where no significant spatial effects appear in the relative noise. The uniformity stems from the geometry of the modelled system: the laterally vibrating fuel rods extend over the full core height, leading to minimal axial spatial dependence. The uniform distribution along the z-direction of the relative noise confirms that a 2D model may be sufficient for a correct representation of the neutron noise behaviour induced by COLIBRI (as shown in Section 4.1).

4.2.2 Neutron noise distribution induced by a POLLEN-like source

In this work, accurate estimates of the cross sections required for modelling POLLEN were not available. Therefore, two different modelling approaches were explored to construct a POLLEN-like perturbation and assess the resulting thermal noise response. In the first approach, the cross section difference in the ϵ/d model discussed in Section 3.2.4 was taken as the difference between the inner-fuel cross section and that of the POLLEN absorber. In the second case, the difference was instead taken between the reflector and the POLLEN absorber.

We consider the experiments with a POLLEN absorber oscillating at a frequency of 1 Hz. The first row in Figure 4.3 shows the thermal noise induced by the reflector-referenced model in the XY plane at the elevation of POLLEN's lower boundary, while the second row shows the YZ plane at the core centre. We see that our POLLEN model induces noise with both lateral and axial spatial dependence. The spatial effects are highly localized near the perturbation boundaries and diminish quickly with distance, approaching nearly zero. The absence of a global, constant background level in the relative noise indicates that our POLLEN-like perturbation does not induce a significant point-kinetic response; rather, its effect is strictly local.

The third and fourth row show the lateral (y-direction) and axial (z-direction) distributions of the static flux and neutron noise for both the reflector- and fuel models. The noise fields have the same spatial shape, but the spatial effects are more pronounced in the reflector model, where the noise amplitude is roughly an order of magnitude larger than the fuel model. This follows directly from the source construction: the reflector differs more from POLLEN in cross section than the inner fuel does.

The axial dependence arises because, unlike COLIBRI, the POLLEN absorber only occupies part of the full core height and is positioned off-centre in the axial direction. The asymmetry generates a noise field with distinct axial features: the noise becomes concentrated at the upper and lower boundaries of the perturbation, while outside these regions both the noise and relative noise are close to zero. Consequently, the POLLEN modelling approaches used here require simulations in full 3D.

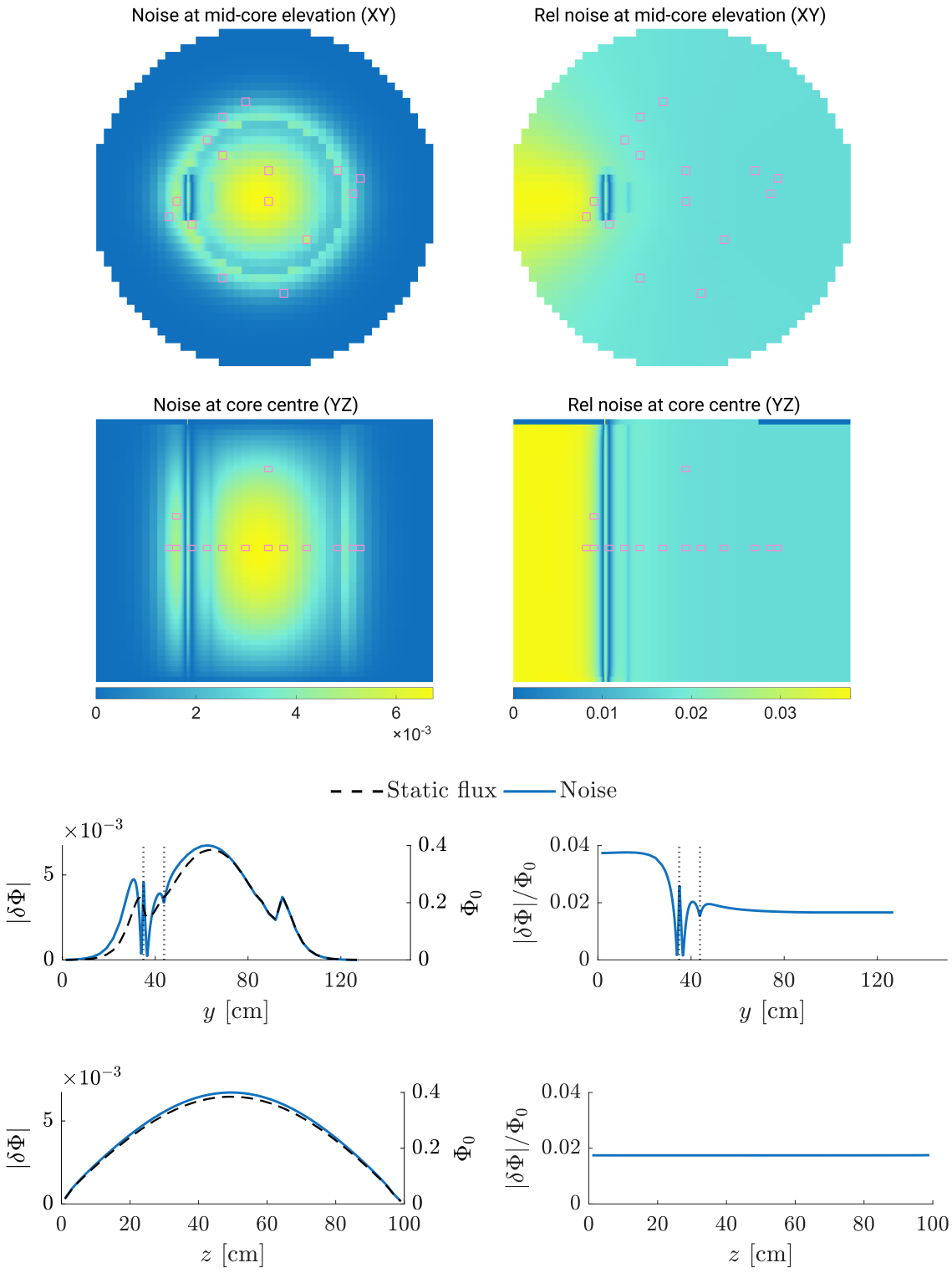

Figure 4.2: Simulated COLIBRI-induced thermal noise: lateral distribution at mid-core elevation (1st row); axial distribution at core centre (2nd row); lateral distribution along y at $x = 64\,\text{cm}$ and $z = 50\,\text{cm}$ (3rd row); axial distribution along z at $x = y = 64\,\text{cm}$ (4th row). The red boxes indicate the locations of the detectors, and the vertical dashed lines in the third row identify the COLIBRI region.

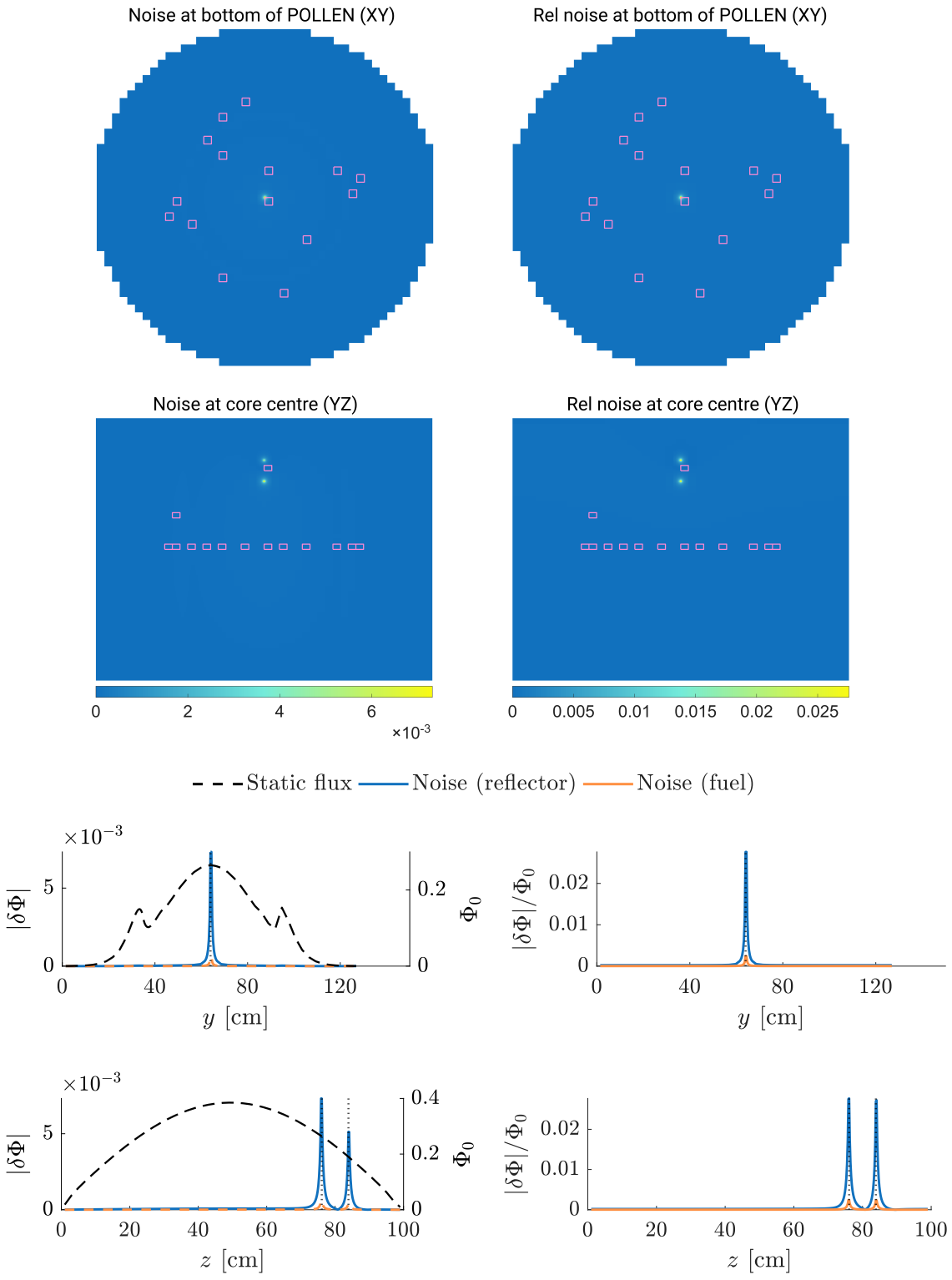

Figure 4.3: Simulated thermal noise induced by a POLLEN-like source: lateral distribution at the height of POLLEN using the reflector model (1st row); axial distribution at core centre using the reflector model (2nd row); lateral distribution along y at $x = 64\,\text{cm}$ and $z = 76\,\text{cm}$ using both models (3rd row); axial distribution along z at $x = y = 64\,\text{cm}$ using both models (4th row). Red boxes indicate detector locations, vertical dashed lines mark the POLLEN boundaries.

4.2.3 Neutron noise distribution induced by COLIBRI combined with a POLLEN-like source

When simulating the experiments where the COLIBRI source and a POLLEN-like central absorber were combined, the fuel-referenced model for the POLLEN-like perturbation lead to a negligible contribution in comparison to the COLIBRI-induced effects. Therefore, we consider only the reflector-referenced model of the POLLEN-like perturbation for the analysis of the neutron noise distribution.

We simulated experiments in which COLIBRI and the POLLEN-like noise source were set to oscillate at a frequency of 1 Hz. By taking the XY plane of the thermal noise amplitude at the height of POLLEN's lower boundary (first row in Figure 4.4) and the YZ plane at the core centre (second row in Figure 4.4), we recognise features originating from both the COLIBRI- and the POLLEN-like perturbation. Specifically the strong local noise gradients near the boundaries of the perturbations and the global background level in the relative noise amplitude induced by COLIBRI.

We examine the lateral (y-direction) and axial (z-direction) distributions of the static flux and neutron noise shown in the third and fourth rows of Figure 4.4. At POLLEN's lower boundary, the noise peak becomes inverted in relation to the corresponding peak produced by the POLLEN-like perturbation alone (see third and fourth row in Figure 4.3). This inversion arises from the global effects introduced by COLIBRI which causes the overall relative noise amplitude to shift to higher values. As a result, this extremum exhibits different characteristics depending on whether COLIBRI is present.

As mentioned in Sec 3.1.3, COLIBRI and POLLEN were set to oscillate in synchronisation in order to enhance the detection of the spatial dependence by reducing the global effect induced by COLIBRI. However, the simulations based on the current POLLEN-like perturbation models provide no clear evidence of such a reduction. Considering this aspect, we adjusted the model of the POLLEN-like perturbation using Eqs. (3.18 – 3.20) discussed in Section 3.2.5, such that it would theoretically counteract the point kinetic component induced by COLIBRI. The calculations of the factor required to rescale the POLLEN-like noise source yielded similar results using the direct and adjoint approaches. As a result, only the results from the direct approach was considered for the analysis of the noise distribution.

The first column of Figure 4.5 shows the amplitude of the thermal noise induced by COLIBRI combined with the rescaled POLLEN model in the XY plane (top) and the YZ plane (bottom). For comparison, the second column shows the noise induced by COLIBRI alone where the point-kinetic component has been manually removed. The removal was done by computing the fundamental reactor mode of the COLIBRI system using Eq. (2.27) and subtracting the product of the resulting

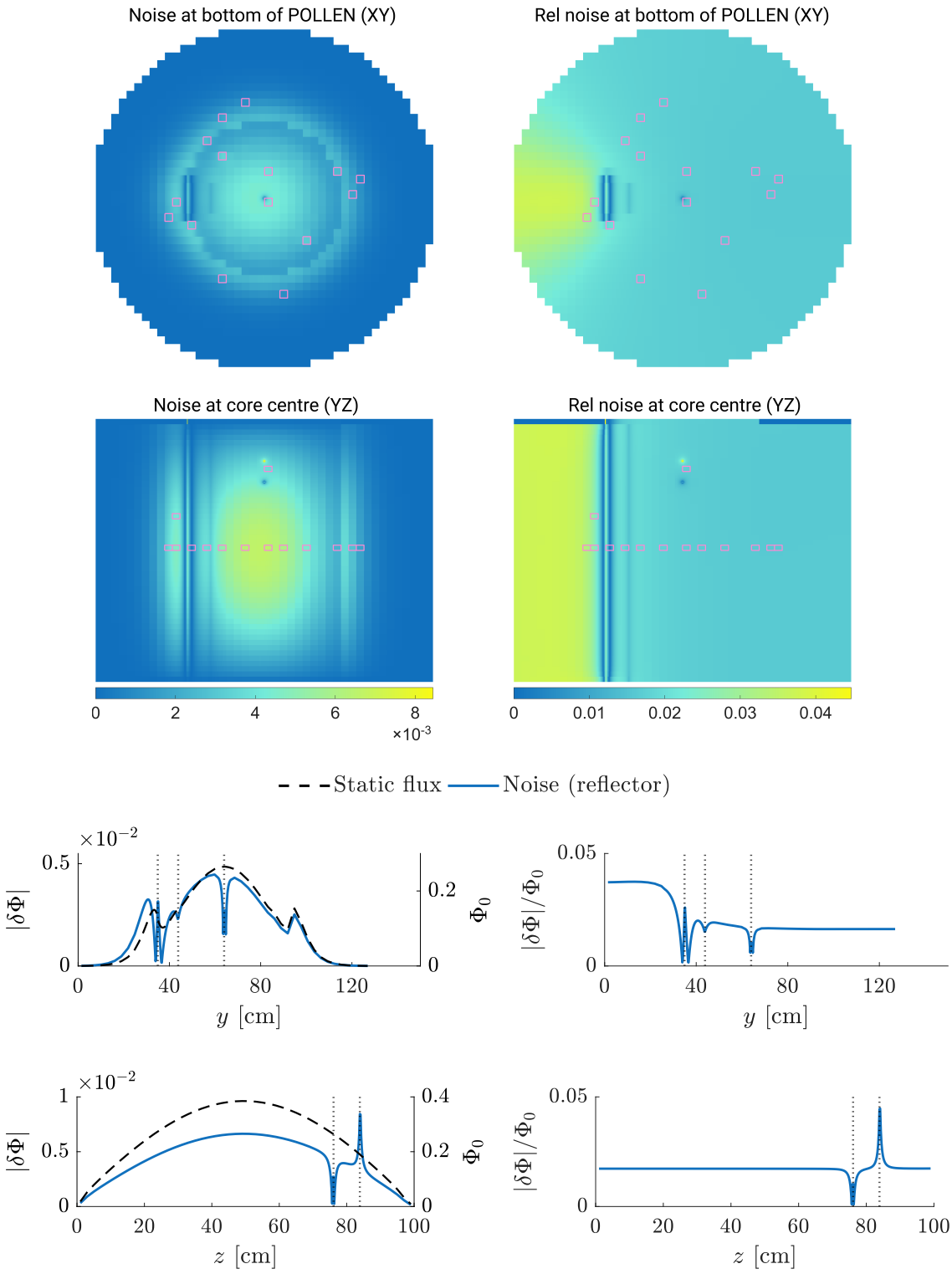

Figure 4.4: Simulated thermal noise induced by COLIBRI combined with the reflector-referenced POLLEN model: lateral distribution at the height of POLLEN (1st row); axial distribution at core centre (2nd row); lateral distribution along y at $x = 64\,\text{cm}$ and $z = 76\,\text{cm}$ (3rd row); axial distribution along z at $x = y = 64\,\text{cm}$ (4th row). The red boxes indicate the locations of the detectors, and the vertical dashed lines in the third and fourth row mark the noise source boundaries.

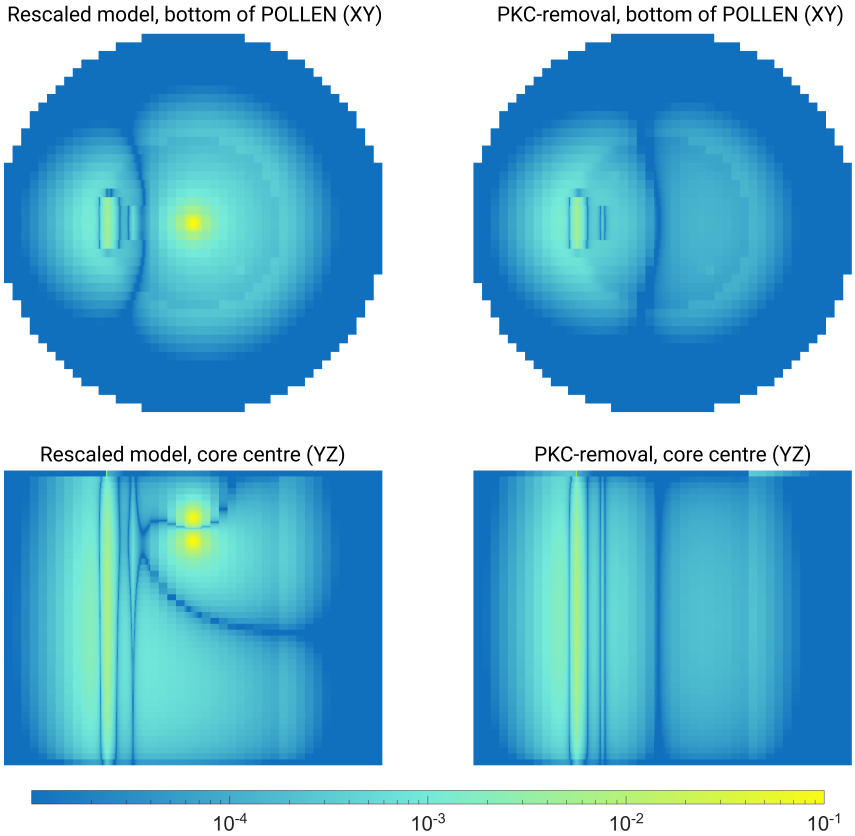

Figure 4.5: Simulated thermal noise induced by COLIBRI combined with the rescaled POLLEN model (1st column) and by COLIBRI with the point-kinetic component (PKC) manually removed (2nd column): lateral distribution at the height of POLLEN (1st row); axial distribution at core centre (2nd row).

factor and the static flux and from the total noise. The scale in the figure is logarithmic to highlight features in low-amplitude regions. Some features appear in both cases. When the point-kinetic contribution is manually removed, a clear region of minimal noise extends vertically across the core. A similar feature is present in the case with the rescaled POLLEN model, although shifted to the left. Additionally, the overall noise levels are comparable in magnitude.

The contribution to the fundamental reactor mode was also computed for the system where COLIBRI was combined with the rescaled POLLEN model. This resulted in essentially zero contribution, which indicates that the rescaled COLIBRI-POLLEN perturbation induces noise dominated by spatial effects rather than a point-kinetic response.

4.2.4 Comparison against experimental data

For the comparison between simulations and experiments in Campaign 3, we consider the quantities discussed in Section 3.1.4: the noise power fractions η_i and $\eta_{i,\mathrm{exp}}$ defined in Eqs. (3.5) and (3.6), which represent the fractional contribution of each de-

tector to the total noise power across all detectors at the perturbation frequency, and the phase $\theta_{i,12}$ relative to detector 12 defined in Eq. (3.4). The simulated quantities were evaluated at the detector volumes presented in Figure 3.7. The results from the direct and adjoint simulations for each noise-source configuration are presented and compared to the experimentally measured MLEs and their corresponding sampled likelihood histograms. Although our models for POLLEN are not fully accurate, we still wanted to examine the discrepancies between the simulations generated by our POLLEN-models and the measured neutron noise induced by the actual POLLEN absorber.

Because the diffusion approximation is expected to produce inaccurate predictions close to the perturbations, the analysis considers both the distribution of the total noise power across all detectors (except detector 3) as well as across the subset of detectors located farther from COLIBRI or POLLEN. Since the noise power fractions (Eqs. (3.5) and (3.6)) depend on the contribution from all included detectors, the resulting fractions differ in amplitude depending on the detector set. Detector 3 was omitted because it consistently measured no response, thus including it would skew the distributions. The detectors are plotted in ascending order of distance from the noise source. In the combined COLIBRI and POLLEN case, the ordering is based on distance from COLIBRI.

Total noise power distributed across detectors

Concerning the COLIBRI case, the simulated fractions for most detectors located in close proximity to the source (8, 14, and 2) differ significantly from the experiments, as shown in the top panel of Figure 4.6. However, for 9 out of 11 detectors located further from the source the responses fall within their sampled likelihood distributions (with slight deviations for detector 15), see bottom panel of Figure 4.6. Here, detectors 11 and 12 are technically outside of their likelihood distributions but the simulated responses are very close to the measured MLEs. Additionally, the corresponding measurement uncertainties are low, resulting in narrow likelihoods.

For the POLLEN-like case, nearly all experimental noise power is concentrated at detector 18, forcing the other detector responses to lower values, shown in the top panel of Figure 4.7. This behaviour is not reproduced by our simulations. Although detector 18 is centred between the perturbation boundaries, much closer to POLLEN than any other detector, its simulated response is nearly zero. This is because the spatial effects induced by our POLLEN models are highly localised to the perturbation boundaries. As shown in the second row of Figure 4.3, the volume of detector 18 is located in an area of relatively low noise, between the two regions where the noise reaches local maxima. Consequently, regardless of which model is used, detector 18 cannot capture those peaks. Additionally, further from the perturbation boundaries the noise is dominated by the static flux, which is relatively low at the height of detector 18. When only considering the subset of detectors further from the noise source (see bottom panel of Figure 4.7), the simulations align well with the experiments, where 11 out of 14 simulations fall within the experimental likelihoods and the remainder are very close to the measured MLE-values.

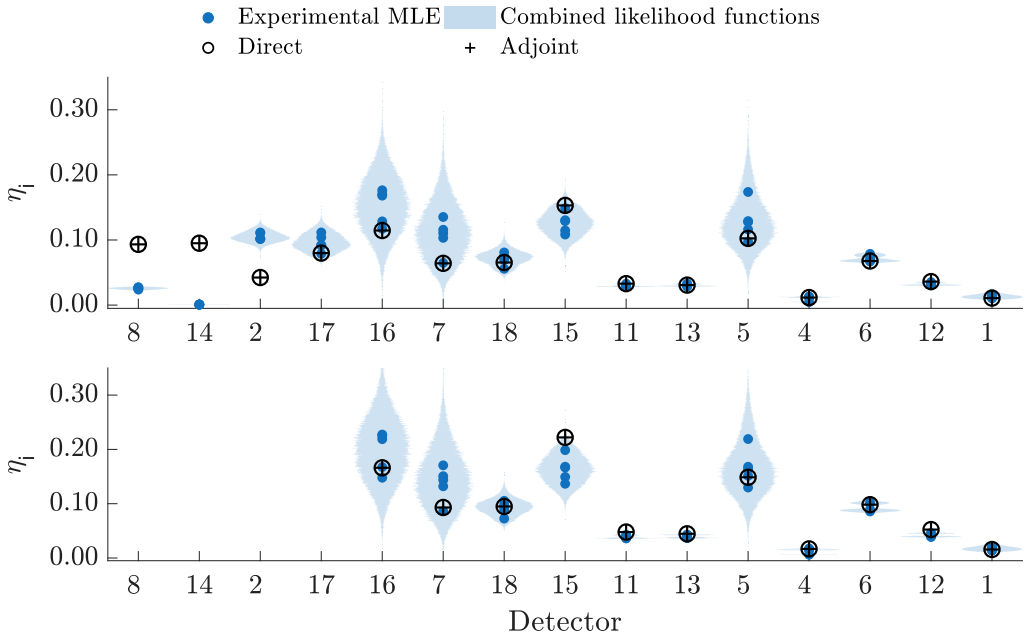

Figure 4.6: Simulated and experimental noise power distributions for the COLIBRI case across all detectors (top), and the subset of detectors located farther from the source (bottom). The experimental data is shown in blue and the simulated responses in black.

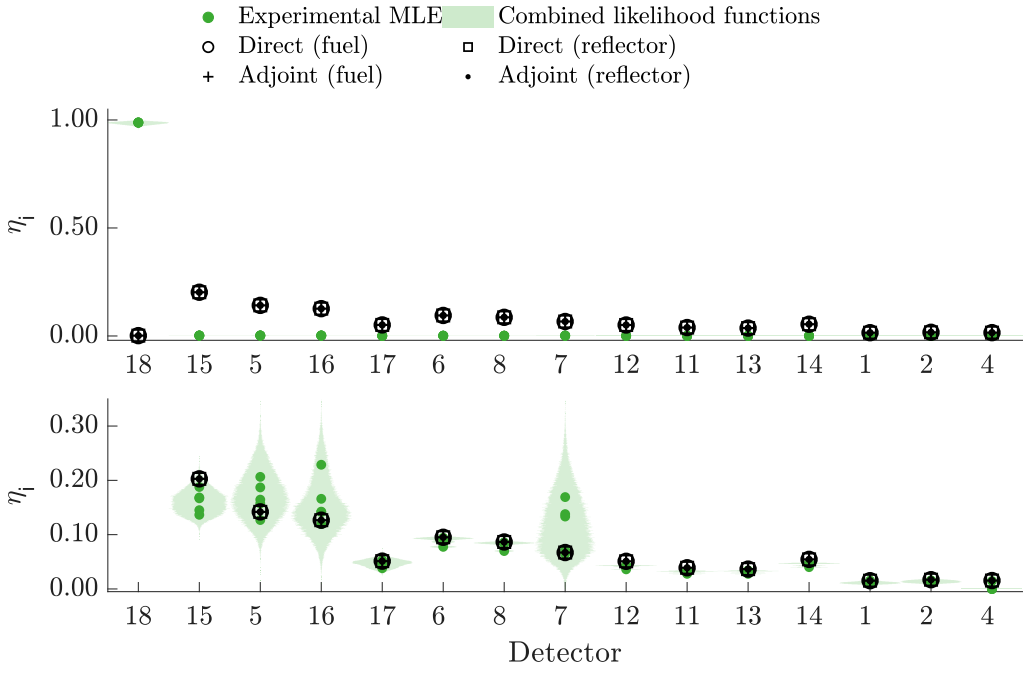

Figure 4.7: Simulated and experimental noise power distribution for the POLLEN case across all detectors (top), and the subset of detectors located farther from the source (bottom). The experimental data is shown in green and the simulated responses in black.

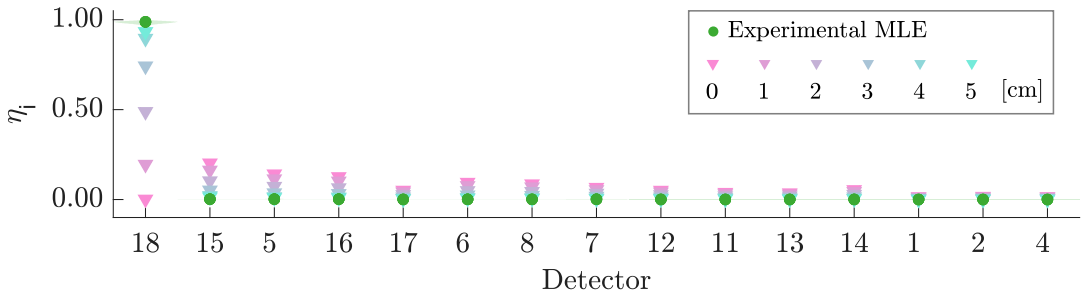

Figure 4.8: Simulated noise power distribution with POLLEN's nominal position shifted. The triangles represent the simulations in which the position of POLLEN was shifted gradually between 0–5 cm above its nominal position of 80 cm. The experimental MLEs are shown as green markers.

It was reported in [14] that during the measurements, POLLEN could erroneously shift its 80 cm nominal position due to a programming issue. This means that it is possible that the boundaries of POLLEN were at times located closer to detector 18 than intended. To test this, we performed simulations where the POLLEN perturbation was gradually shifted upwards, thus reducing the distance between POLLEN's lower boundary and the detector 18 volume 1 cm at a time. This resulted in the simulated responses for detector 18 progressively approaching the measured response, as demonstrated in Figure 4.8. The highest simulated noise power fraction, and thus the lowest deviation from measurements was reached at a nominal position of 85 cm. Shifting it further resulted in a decreasing fraction. These results demonstrate that the relative position of the POLLEN-like perturbation with respect to the detectors has a large impact on the simulated responses, and our sensitivity analysis indicates that a shift of approximately 5 cm is required for the simulated distribution to resemble the experimental one.

When considering the combined COLIBRI and POLLEN case, the experimental distribution of the total noise power across the detectors is dominated by detector 18, while the remaining detectors only contribute with small fractions, see the top panel of Figure 4.9. The corresponding simulated distributions generated by the POLLEN-like perturbations are significantly lower, especially in the case of the reflector-based model. This model yields a distribution that is essentially identical to that of COLIBRI alone (shown in the top panel of Figure 4.6). This implies that the effect of the selected POLLEN-like perturbation is minimal compared to that of COLIBRI at the specific detector locations, which may depend on the fact that the detector locations do not correspond to the regions where the induced noise reaches local maxima.

When detectors near the source are excluded from the analysis, the simulations generally agree with the experimental measurements, see bottom panel in Figure 4.9. For the reflector model and the rescaled POLLEN model, 8 out of 10 and 7 out of 10 simulated responses fall within their respective likelihood distributions, respectively. The remainder fall just outside. The reflector-model simulations are in better agreement with the experimental data for detectors far from the source, while

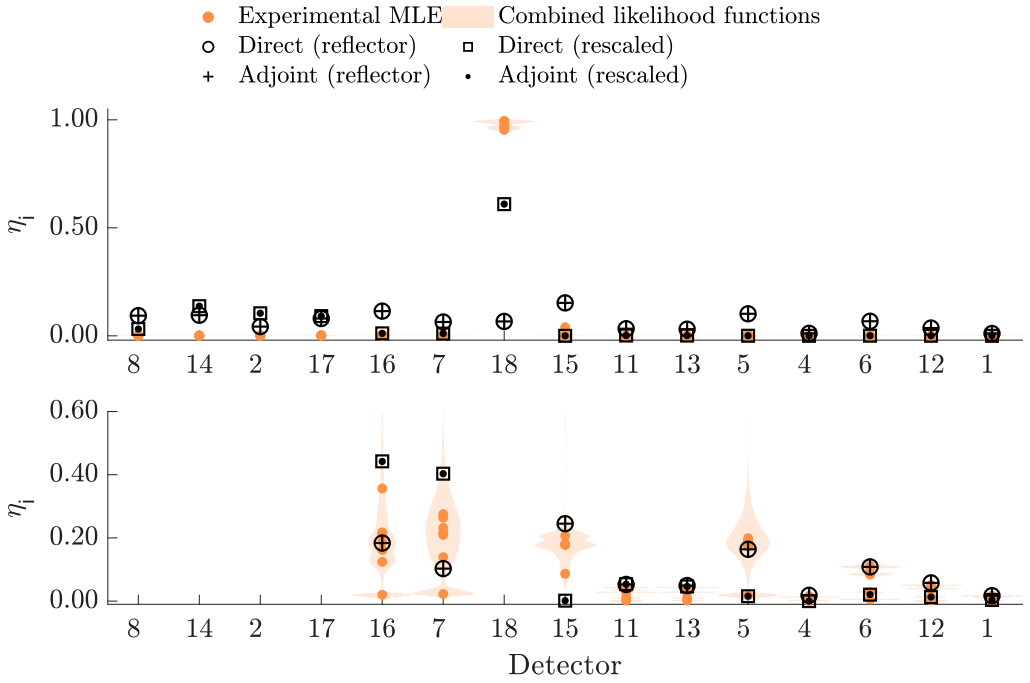

Figure 4.9: Simulated and experimental noise power distribution for the case of COLIBRI combined with POLLEN across all detectors (top), and the subset of detectors located farther from the source (bottom). The experimental data is shown in orange and the simulated responses in black.

the rescaled POLLEN model simulates a response closer to the experimental value for detector 18. For several detectors, the measured MLE values are more scattered than those obtained from experiments with COLIBRI and POLLEN applied separately. This results in wider, multimodal likelihood distributions, especially evident for detectors 16, 7, 15, 5 (and 6 to some extent).

Consistent across all noise source configurations is that the direct and adjoint approaches yield simulated results that are very similar to each other for all detectors, as shown in Figures 4.6 – 4.9. Another trend that persists across all configurations is that, for detectors located in close proximity to the noise source, the simulated noise power fractions differ significantly from the experiments. This is perhaps most easily recognised in the COLIBRI case shown in the top panel of Figure 4.6. This stems from the underlying approximations implemented by the solver, specifically the diffusion approximation and its limited ability to accurately describe neutron transport in the vicinity of a noise source, as stated in Section 2.2. Near a localised source, the neutron flux exhibits strong spatial variations and a significant angular dependence, i.e. it becomes anisotropic [27, p. 138]. When the diffusion approximation is applied, the flux is assumed to be isotropic and higher order angular information is discarded. Additionally, it is assumed through Fick's law that the neutron flux varies slowly with position [25, p. 125]. Consequently, diffusion theory cannot accurately capture the highly directional or rapidly varying flux gradients that occur near a noise source.

For the detectors located farther from the noise sources, the simulated responses closely follow the shape of the static flux displayed in Figure 3.9 and thus are nearly point-kinetic in character. This is confirmed by the fact that, in these reactor regions, the calculated relative noise amplitudes are nearly constant, as shown in Figures 4.2 – 4.4.

Phase analysis

In every analysed experiment, the calculated phases for all detectors are very close to the calculated phase of detector 12 (which was used as reference) resulting in a relative phase of approximately zero across all detectors, with the exception of the case where COLIBRI was combined with the rescaled model for the POLLEN-like perturbation. This is shown in Figure 4.10 where the simulated relative phases are plotted in black. In the experimental data for the separate COLIBRI and POLLEN cases (panel 1 and 2), phase shifts are observed for some detectors. These phase shifts are unique to the specific noise source and are consistent across individual measurements. For the COLIBRI case, deviations between measured and simulated responses occur for detectors 14 and 17. A similar phase shift is observed for detector 14 in Campaign 2, as shown in Figure 4.1. For the POLLEN case, the response for detector 18 differs. These deviations suggest that the phase behavior cannot be reproduced because of modelling limitations.

In the COLIBRI case, for the detectors close to the source (8, 14, 2, and 17), none of the simulated phases fall within their respective experimental likelihood. For the subset of detectors located far from the source however, the simulations agree quite well with the experiments. 8 out of 11 simulated responses fall within the corresponding likelihood distributions, and the remainder are very close to the measured MLEs.

For the simulations of POLLEN-like perturbations, a small negative phase shift is observed for detector 18. This behaviour somewhat resembles the measurements, where most detectors measure only small phases except for detector 18 and 4. The simulations are in reasonable agreement with the experiments, where 10 out of 15 simulated responses fall within the corresponding likelihoods. Detectors 15, 17, 6, and 8 are technically outside the distributions, however, they lie in-between densely arranged modes.

A considerable spread between the measured MLE-values is observed for the COLIBRI + POLLEN case, where most of the sampled likelihood distributions are multimodal with distinct modes that show little or no overlap. This makes it challenging to evaluate the consistency between simulations and experiments. Regarding the simulations where a POLLEN-like perturbation was rescaled to remove the point-kinetic component of the noise induced by COLIBRI, a phase shift of π relative to detector 12 is observed for most detectors, with detectors 5, 4, 6, and 1 being the exceptions. A deeper investigation is required to determine the underlying cause of the observed phase shift, as this aspect was not investigated here.

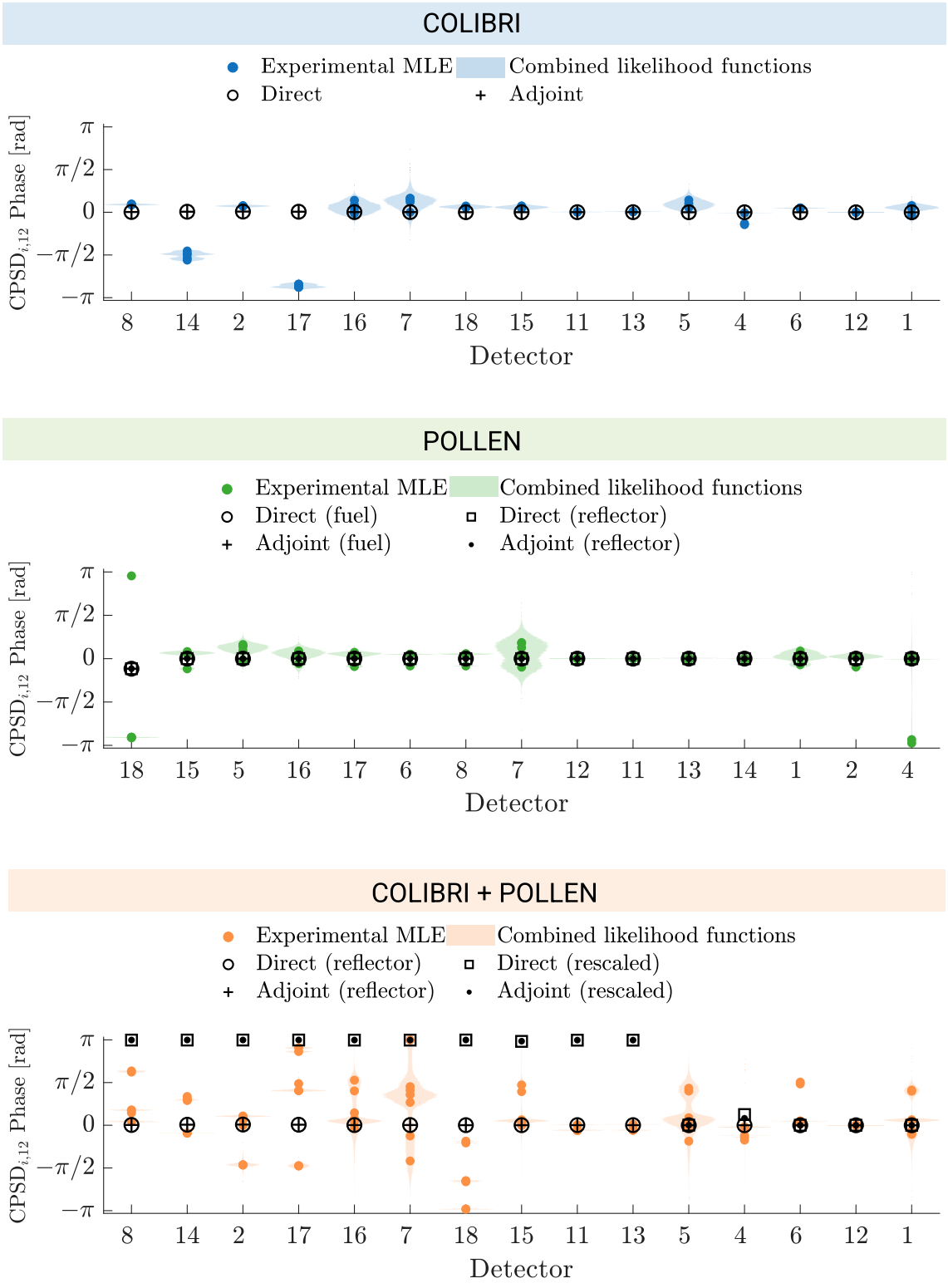

Figure 4.10: Simulated and experimental phases relative to detector 12 for COLIBRI (top), POLLEN (middle), and COLIBRI combined with POLLEN (bottom). The simulated values are shown as black markers, and the experimental values as coloured markers.

5

Conclusions and outlook

This work revolved around modelling and simulating the neutron noise experiments carried out at the CROCUS reactor at EPFL. Three noise source configurations were studied: (i) a laterally vibrating group of fuel rods (COLIBRI), (ii) an axially vibrating absorber rod (POLLEN), and (iii) a combination of the two aforementioned noise sources. The purpose was to investigate the modelling of these experiments using the neutron noise solver CORE SIM+ and exploring modelling options for POLLEN-like perturbations. The study presented in this thesis led to insightful results, which may lay the ground for future investigations.

Two different methods for computing the thermal noise distribution in the reactor was used: the direct approach in which the first-order neutron noise equation is solved to obtain the response to a given noise source across the entire reactor core, and the adjoint approach in which adjoint operators are utilized to compute the noise response at prescribed locations in the reactor to any perturbation. Both approaches yielded consistent results for all simulated cases. Regarding the 2D and 3D simulations using a COLIBRI perturbation, the simulated detector responses were virtually identical across all detectors. This was expected since the fuel rods extend across the full core height and the movement is uniform in the axial direction.

The COLIBRI simulations resulted in noise fields with lateral spatial effects near the perturbation boundaries, as well as a global point-kinetic response of the reactor. We tested various models for a POLLEN-like perturbation. In the first approach, the cross section difference used in the ϵ/d model was taken as the difference between the cross section associated with the inner-fuel region and that of the POLLEN absorber. In the second case, the difference was instead taken between the reflector region and the POLLEN absorber. Both models produced noise fields with strong spatial features highly localised to the immediate surrounding of the perturbation boundaries. The noise fields were identical in shape for the two models, but with an amplitude approximately one order of magnitude larger for the reflector model. Due to the axial and lateral spatial dependence, our POLLEN-modelling approach require simulations in full 3D.

We studied the case of COLIBRI combined with a POLLEN-like perturbation. In addition to the two models above, we also considered a model where a POLLEN-like perturbation is tuned to remove the point-kinetic component of the noise induced by COLIBRI, thus extracting the spatial contribution from the total noise. The global effects caused by COLIBRI was successfully reduced after introducing the rescaled POLLEN-like perturbation to the system. This is in comparison to the unscaled POLLEN-like sources, where the POLLEN-induced effects using the fuel-referenced model became obscured by the much stronger COLIBRI-induced noise, while the reflector-referenced model showed features originating from both noise sources, but with a visible point-kinetic component induced by COLIBRI.

When considering the noise in the detector volumes, we found that the simulated responses at detector locations further from the perturbation generally agree well with the experimentally measured noise. In these regions, the noise field is dominated by the fundamental reactor mode, meaning the response is essentially point-kinetic in character. On the contrary, in the vicinity of the noise source the deviations between simulated and measured noise are significant. One reason for these deviations is related to the underlying approximations of the diffusion solver that lead to inaccurate predictions of the spatial gradients of the noise close to a perturbation. For the POLLEN case, the POLLEN-like models used to simulate the perturbation are approximations that do not fully describe the physics and thus contribute to the discrepancies against the experimental data. The simulated phases are approximately zero across all detectors for all noise source configurations. This is somewhat reflected in the experimental data, where most measured phases are relatively small. However, deviations between measured and simulated data are observed for detectors near the source, suggesting that there is some underlying phase behaviour that we were unable to reproduce.

Despite the discrepancies, the comparison between the measurements of the noise induced by the real POLLEN device and the results obtained from simulating the vibration of an absorber at the location of POLLEN shows similarities that can help in the development of models for this type of scenario. A natural step for future work will be to derive accurate cross sections for the CROCUS configuration with POLLEN, and develop a proper model of POLLEN that can be used for neutron noise simulations of these experiments.

It would be valuable to investigate the underlying reason for the non-zero relative phase of some of the detectors in the experimental data. This would shed light on potential modifications that can be made to our modelling approach, hopefully leading to a better reflection of the spatial variations of the phase in the reactor.

For the assessment of neutron noise solvers such as CORE SIM+, additional experiments are highly desirable. Experiments with multiple perturbations that generate more complex spatial noise distributions would be particularly valuable. For the validation of more accurate POLLEN models, experiments performed with multiple detectors placed closer to the perturbation and with varying core elevations that

provide information about the axial structure of the noise could prove useful.

Even though the solver does not fully predict the noise in the vicinity of a noise source, it seems to accurately model the spatial extent of the noise. Meaning that detectors that have a strong point-kinetic response are also simulated as such, whereas detectors that show a spatial response also does so in the simulations. It would potentially be interesting to investigate whether this property can be used to infer the location of sources without having to simulate the noise fields themselves, and instead consider the combined field of view of detectors that measure a spatial response. A relevant aspect would also be to identify possible regions in the system where solvers provide more accurate estimates of the noise and still retain relevant spatial information.

Bibliography

[1] L. Meitner and O. R. Frisch, "Disintegration of uranium by neutrons: A new type of nuclear reaction," *Nature*, vol. 143, no. 3615, pp. 239–240, 1939. DOI: 10.1038/143239a0. [Online]. Available: https://doi.org/10.1038/143239a0.

[2] R. A. Knief, *Nuclear Fission Power Plants*, R. A. Meyers, Ed. New York, NY: Springer New York, 2012, pp. 7086–7141, ISBN: 978-1-4419-0851-3. DOI: 10.1007/978-1-4419-0851-3_22. [Online]. Available: https://doi.org/10.1007/978-1-4419-0851-3_22.

[3] J. C. Lee, *Nuclear Reactor Physics and Engineering*. John Wiley & Sons, 2020, ISBN: 978-1-119-58232-8. [Online]. Available: https://app.knovel.com/hotlink/pdf/id:kt012EV982/nuclear-reactor-physics/nuclear-power-plants.

[4] IAEA. "PRIS - Power Reactor Information System," Accessed: Apr. 22, 2026. [Online]. Available: https://pris.iaea.org/PRIS/home.aspx.

[5] IAEA. "In Operation & Suspended Operation Reactors," Accessed: Apr. 22, 2026. [Online]. Available: https://pris.iaea.org/PRIS/WorldStatistics/OperationalReactorsByType.aspx.

[6] IAEA. "Country Statistics Sweden," Accessed: Apr. 22, 2026. [Online]. Available: https://pris.iaea.org/PRIS/CountryStatistics/CountryDetails.aspx?current=SE.

[7] Regeringskansliet. "Frågor och svar om kärnkraft," Accessed: Apr. 22, 2026. [Online]. Available: https://www.regeringen.se/regeringens-politik/energi/fragor-och-svar-om-karnkraft/.

[8] Regeringskansliet. "Internationellt samarbete för att tredubbla den globala produktionen av kärnkraft," Accessed: Apr. 22, 2026. [Online]. Available: https://www.regeringen.se/regeringens-politik/energi/fragor-och-svar-om-karnkraft/.

[9] European Horizon 2020 CORTEX. "About CORTEX," Accessed: Apr. 23, 2026. [Online]. Available: http://cortex-h2020.eu/about-cortex/.

[10] European Horizon 2020 CORTEX. "Objectives," Accessed: Apr. 23, 2026. [Online]. Available: https://cortex-h2020.eu/objectives/.

[11] EPFL. "CROCUS Reactor," Accessed: Apr. 23, 2026. [Online]. Available: https://www.epfl.ch/labs/lrs/facilities/crocus-reactor/.

[12] V. Lamirand et al., "Experimental Report of the 1st Campaign at AKR-2 and CROCUS," EPFL, Deliverable D2.1, Dec. 3, 2018.

[13] V. Lamirand et al., "Experimental report of the 2nd campaign at AKR-2 and CROCUS," EPFL, Deliverable D2.2, Mar. 11, 2021.

[14] V. Lamirand, A. Knospe, K. Ambrozic, F. Vitullo, and C. Lange, "Experimental report of the 3rd campaign at AKR-2 and CROCUS," EPFL, Deliverable D2.4, Aug. 30, 2021.

[15] C. Demazière, *Power reactor noise theory*, Presentation at the 2nd CORTEX Validation Workshop, Online workshop, 23–24 March 2021, 2021. [Online]. Available: https://cortex-h2020.eu/workshop-training/materials/#3.

[16] R. Gross, D. Tomatis, and E. Gilad, "High-accuracy neutron diffusion calculations based on integral transport theory," *European Physical Journal Plus*, vol. 135, p. 235, 2020. DOI: 10.1140/epjp/s13360-020-00216-y.

[17] A. G. Mylonakis, P. Vinai, and C. Demazière, "Core sim+: A flexible diffusion-based solver for neutron noise simulations," *Annals of Nuclear Energy*, vol. 155, p. 108 149, 2021, ISSN: 0306-4549. DOI: https://doi.org/10.1016/j.anucene.2021.108149. [Online]. Available: https://www.sciencedirect.com/science/article/pii/S0306454921000256.

[18] C. Demazière, "CORE SIM: A multi-purpose neutronic tool for research and education," *Annals of Nuclear Energy*, vol. 38, no. 12, pp. 2698–2718, 2011, ISSN: 0306-4549. DOI: https://doi.org/10.1016/j.anucene.2011.06.010. [Online]. Available: https://www.sciencedirect.com/science/article/pii/S0306454911002210.

[19] A. G. Mylonakis et al., "Core sim+ simulations of colibri fuel rods oscillation experiments and comparison with measurements," *EPJ Web of Conferences*, vol. 247, p. 21 006, Jan. 2021. DOI: 10.1051/epjconf/202124721006.

[20] P. Vinai et al., "Final validation report," Chalmers University of Technology, Deliverable D2.5, Aug. 30, 2021.

[21] M. Bahrami and N. Vosoughi, "Sn transport method for neutronic noise calculation in nuclear reactor systems: Comparative study between transport theory and diffusion theory," *Annals of Nuclear Energy*, vol. 114, pp. 236–244, 2018, ISSN: 0306-4549. DOI: https://doi.org/10.1016/j.anucene.2017.12.041. [Online]. Available: https://www.sciencedirect.com/science/article/pii/S0306454916310209.

[22] A. Mylonakis, H. Yi, P. Vinai, and C. Demazière, "Neutron noise simulations in a heterogeneous system: A comparison between a diffusion-based and a

discrete ordinates solver," in *Mathematics & Computational Methods Applied to Nuclear Science & Engineering (M&C 2019)*, Presented at M&C 2019, Portland, Oregon, USA, Aug. 2019. DOI: 10.5281/zenodo.3567577.

[23] G. I. Bell and S. Glasstone, *Nuclear Reactor Theory*. Krieger Publishing Company, 1970, ISBN: 0-88275-790-3.

[24] C. Demazière, *Modelling of Nuclear Reactor Multi-physics*. Academic Press, 2020, ISBN: 978-0-12-815069-6. DOI: 10.1016/C2017-0-01631-2.

[25] J. R. Lamarsh, *Introduction to Nuclear Reactor Theory* (Addison-Wesley Series on Nuclear Engineering). Addison-Wesley Publishing Company, 1966, ISBN: 9780201041200.

[26] J. R. Lamarsh and A. J. Baratta, *Introduction to Nuclear Engineering*, 3rd ed. Prentice Hall, 2001, ISBN: 0-201-82498-1.

[27] J. J. Duderstadt and L. J. Hamilton, *Nuclear Reactor Analysis*. Wiley, 1976, ISBN: 9788126541218.

[28] I. Pázsit and C. Demazière, "Noise techniques in nuclear systems," in *Handbook of Nuclear Engineering*, D. G. Cacuci, Ed. Boston, MA: Springer US, 2010, pp. 1629–1737, ISBN: 978-0-387-98149-9. DOI: 10.1007/978-0-387-98149-9_14. [Online]. Available: https://doi.org/10.1007/978-0-387-98149-9_14.

[29] V. Larsson and C. Demazière, "Comparative study of 2-group p1 and diffusion theories for the calculation of the neutron noise in 1d 2-region systems," *Annals of Nuclear Energy*, vol. 36, no. 10, pp. 1574–1587, 2009, ISSN: 0306-4549. DOI: https://doi.org/10.1016/j.anucene.2009.07.009. [Online]. Available: https://www.sciencedirect.com/science/article/pii/S0306454909002217.

[30] M. Hursin et al., "Modeling noise experiments performed at akr-2 and crocus zero-power reactors," *Annals of Nuclear Energy*, vol. 194, p. 110 066, 2023, ISSN: 0306-4549. DOI: https://doi.org/10.1016/j.anucene.2023.110066. [Online]. Available: https://www.sciencedirect.com/science/article/pii/S0306454923003857.

[31] K. V. Mardia and P. E. Jupp, *Directional Statistics* (Wiley Series in Probability and Statistics). John Wiley & Sons, 1999, ISBN: 9780471953333. DOI: 10.1002/9780470316979.

[32] Demazière, C et al., "Neutron noise-based anomaly classification and localization using machine learning," *EPJ Web Conf.*, vol. 247, p. 21 004, 2021. DOI: 10.1051/epjconf/202124721004. [Online]. Available: https://doi.org/10.1051/epjconf/202124721004.

A

Definitions of $\boldsymbol{\Sigma}_{dyn}, \boldsymbol{\phi}_a, \boldsymbol{\phi}_r$, and $\boldsymbol{\phi}_f$

In the first-order neutron noise equations, Eq. (2.20–2.21), the matrices and vectors $\boldsymbol{\Sigma}_{dyn}, \boldsymbol{\phi}_a, \boldsymbol{\phi}_r$, and $\boldsymbol{\phi}_f$ have the following definitions [17, Eqs. (A.1–A.5)].

The matrix $\boldsymbol{\Sigma}_{dyn}(\boldsymbol{r}, \omega)$ is defined as

$$\boldsymbol{\Sigma}_{dyn}(\boldsymbol{r}, \omega) \equiv \begin{bmatrix} -\Sigma_1(\boldsymbol{r}, \omega) & \dfrac{\nu\Sigma_{f,2,0}(\boldsymbol{r})}{k_{\text{eff}}}\left(1 - \dfrac{i\omega\beta}{i\omega + \lambda}\right) \\ \Sigma_{r,0}(\boldsymbol{r}) & -\left(\Sigma_{a,2,0}(\boldsymbol{r}) + \dfrac{i\omega}{v_2}\right) \end{bmatrix} \tag{A.1}$$

with

$$\Sigma_1(\boldsymbol{r}, \omega) \equiv \Sigma_{a,1,0}(\boldsymbol{r}) + \frac{i\omega}{v_1} + \Sigma_{r,0}(\boldsymbol{r}) - \frac{\nu\Sigma_{f,1,0}(\boldsymbol{r})}{k_{\text{eff}}}\left(1 - \frac{i\omega\beta}{i\omega + \lambda}\right). \tag{A.2}$$

The column vector $\boldsymbol{\phi}_r(\boldsymbol{r})$ and the matrices $\boldsymbol{\phi}_a(\boldsymbol{r})$ and $\boldsymbol{\phi}_f(\boldsymbol{r}, \omega)$ all contain the static fluxes and are defined in the following ways

$$\boldsymbol{\phi}_r(\boldsymbol{r}) \equiv \begin{bmatrix} \phi_{1,0}(\boldsymbol{r}) \\ -\phi_{1,0}(\boldsymbol{r}) \end{bmatrix} \tag{A.3}$$

$$\boldsymbol{\phi}_a(\boldsymbol{r}) \equiv \begin{bmatrix} \phi_{1,0}(\boldsymbol{r}) & 0 \\ 0 & \phi_{2,0}(\boldsymbol{r}) \end{bmatrix} \tag{A.4}$$

$$\boldsymbol{\phi}_f(\boldsymbol{r}, \omega) \equiv \begin{bmatrix} -\dfrac{\phi_{1,0}(\boldsymbol{r})}{k_{\text{eff}}}\left(1 - \dfrac{i\omega\beta}{i\omega + \lambda}\right) & -\dfrac{\phi_{2,0}(\boldsymbol{r})}{k_{\text{eff}}}\left(1 - \dfrac{i\omega\beta}{i\omega + \lambda}\right) \\ 0 & 0 \end{bmatrix} \tag{A.5}$$

B

Detector positions

Table B.1 shows the detector coordinates of the thermal detectors that were used in this work, also illustrated in Figure 3.3. A small number of detector coordinates in the experimental documentation were found to be inconsistent with the physical detector locations shown in the detector maps or the descriptions found in text. These coordinates were therefore adjusted, which are indicated in the table.

Table B.1: Coordinates for the thermal detectors in the three campaigns.

Det. Num.	C1			C2			C3		
	North	**East**	**Axial**	**North**	**East**	**Axial**	**North**	**East**	**Axial**
1	8.7	35.8	50.0	8.7	35.8	50.0	8.7	35.8	50.0
2	-8.7	-35.8	50.0	-8.7	-35.8	50.0	-8.7	-35.8	50.0
3	36.35	-8.6	50.0	36.35	-8.6	50.0	36.35	-8.6	50.0
4	-36.35	8.6	50.0	-36.35	8.6	50.0	-36.35	8.6	50.0
5	-14.7	29.8	50.0	16.0	-16.0	50.0	-16.0	16.0	50.0
6	15.4	-29.8	50.0	10.2	27.7	50.0	10.2	27.7	50.0
7	16.04	-16.04	50.0	-16.0	16.0	50.0	21.8	-21.8	50.0
8	-10.21	-27.71	50.0	-10.2	-27.7	50.0	-10.2	-27.7	50.0
9	27.71	10.21	50.0	-	-	-	-	-	-
10	-27.71	-20.21	50.0	-	-	-	-	-	-
11	0.0	0.0	50.0	29.5	-14.6	50.0	29.5	-14.6	50.5
12	-	-	-	2.8	32.4	50.0	2.8	32.4	50.5
13	-	-	-	-29.5	-14.7	50.0	-29.5	-14.7	50.5
14	-	-	-	-2.5	-33.1	50.0	-2.5	-33.1	50.5
15	-	-	-	0.0	0.0	50.0	11.5	0.0	50.0
16	-	-	-	-	-	-	16.0*(-16.0)	-16.0*(16.0)	50.0
17	-	-	-	-	-	-	0.0	-34.3*(34.3)	62.0
18	-	-	-	-	-	-	-0.5*(-7.0)	0.0	80.0

Coordinates are given in cm. The origin in the horizontal plane (North/East) is set at the geometric centre of the core.

* Adjusted values. Reported values from the experimental documentation are shown in parentheses.

CHALMERS UNIVERSITY OF TECHNOLOGY
Gothenburg, Sweden
www.chalmers.se

UNIVERSITY OF
GOTHENBURG

CHALMERS
UNIVERSITY OF TECHNOLOGY